

**DESIGN AND CHARACTERIZATION OF A
PRESSURE DIFFERENTIAL TRAPPING
MECHANISM FOR SUSPENDED MICRO-PARTICLES
IN A MICRO-FLUIDIC DEVICE**

by

Alvin O. Cruz Díaz

A thesis submitted in partial fulfillment of the requirements for the degree of

MASTER OF SCIENCE
in
MECHANICAL ENGINEERING

UNIVERSITY OF PUERTO RICO
MAYAGÜEZ CAMPUS
2012

Approved by:

Pedro Quintero, PhD
Member, Graduate Committee

Date

Ricky Valentín, PhD
Member, Graduate Committee

Date

Rubén Díaz-Rivera, PhD
President, Graduate Committee

Date

Lic. Elvia Camayd
Representative of Graduate Studies

Date

Gustavo Gutierrez, PhD
Chairperson of the Department

Date

ABSTRACT

The increasing interest for dedicated analysis of single particles at microscopic scales, such as biological cells, has led researchers to create micro-fluidic systems capable of trapping particles in a liquid flow. The present study tests a device that employs a pressure difference trapping mechanism to isolate suspended micro-particles. The studied micro-fluidic device was fabricated using typical soft lithography and consists of parallel canals that are linked by small apertures that function as localized pressure-gradient traps. Experiments to characterize the functionality of the trapping sites of the device were conducted using polystyrene beads. These experiments consisted of using 20 μm polystyrene beads suspended in PBS, which were introduced using a syringe pump, while one outlet port of the device was controlled to produce an outflow rate of 25%, 50%, 62.5% and 75% of the inflow rate. Another case in which the outlet remained at atmospheric pressure was also studied. The experiments performed with 20 μm beads demonstrated that the apertures were capable of trapping and retaining the beads. A micro-PIV was used to characterize the flow and the velocity profile in different parts of the device. The results from the micro-PIV experiments were used to validate a computational fluid dynamics model using COMSOL Multiphysics. The experiments show that the trapping efficiency is a strong function of the controlled output flow suggesting that the functionality of the device could be manipulated with a variable fluidic resistance. It was also found that the velocity profile of the computational model agrees well with experiments carried out with the micro-PIV, but only when there is slip at the PDMS walls. We suspect that the velocity slip is due to the surface treatment of

the microchannel walls (air plasma followed by bovine serum albumin functionalization). However, the evidence is not conclusive. The validated computational model presented in this study will serve as a stepping stone for the development of high-density cell isolation micro-devices for high-throughput single-cell electroporation applications and the detection of circulating tumor cells.

RESUMEN

El creciente interés para el análisis dedicado de partículas individuales a escalas microscópicas, tales como las células biológicas, ha llevado a los investigadores a crear sistemas micro-fluídicos capaces de atrapar partículas suspendidas en un flujo. El presente estudio coloca a prueba un dispositivo que utiliza una diferencia de presión como mecanismo para aislar micro-partículas suspendidas. El dispositivo micro-fluidico fue fabricado utilizando litografía blanda y consiste de canales paralelos que están unidos por pequeñas aberturas que funcionan como trampas de gradiente de presión. Los experimentos para caracterizar la funcionalidad de los sitios de captura del dispositivo se realizaron utilizando esferas de poliestireno. Estos experimentos consistieron en utilizar esferas de poliestireno 20 μm suspendidos en PBS, que se introducen mediante una bomba de jeringa, mientras que un puerto de salida del dispositivo fue controlado para producir una razón de flujo de salida de 25%, 50%, 62.5% y 75% de la razón de flujo de entrada. Además se estudio un caso en el que la salida se mantuvo a presión atmosférica. Los experimentos realizados con esferas de 20 μm demostraron que las aberturas eran capaces de atrapar y retener las esferas. Un micro-PIV se utilizó para caracterizar el flujo y el perfil de velocidad en diferentes partes del dispositivo micro-fluidico. Los resultados de los experimentos de micro-PIV fueron utilizados para validar un modelo computacional para el cual se utilizó COMSOL Multiphysics. Los experimentos muestran que la eficiencia de captura es una fuerte función del flujo de salida controlado que sugiere que la funcionalidad del dispositivo podría ser manipulado con una resistencia fluidica variable. También se encontró que el perfil de

velocidad del modelo computacional concuerda bien con los experimentos llevados a cabo con el micro-PIV, pero sólo cuando hay deslizamiento en las paredes de PDMS. Se sospecha que el deslizamiento de velocidad es debido al tratamiento superficial de las paredes de los micro-canales (plasma de aire seguido por funcionalización con suero albumino de bovino). Sin embargo, la evidencia no es concluyente. El modelo computacional validado en este estudio servirá como un trampolín para el desarrollo de micro-dispositivos de alta densidad de celdas de aislamiento para aplicaciones de alto rendimiento de electroporación de una sola célula y la detección de células cancerígenas suspendidas en un fluido.

To my family . . .

ACKNOWLEDGEMENTS

I want to thank God for giving me the gift of life. Also, he has giving me the strength and the courage to fight for my goals. I will like to thank my family that without their love, dedication and support I will not be here. I want to express my gratitude to Dr. Ruben Díaz-Rivera, my advisor, for giving me the opportunity to work with him. I am grateful for his advice and his support not only in the academic and research level but also in a personal level. He helped me grow as a professional and I will always be grateful for that. I also want to thank Dr. Pedro Quintero, Dr. Ricky Valentín and Dr. Paul Sundaram for their assistance and advice with my research. I want to thank all my friends for their support and for being there when I needed them. People come and go but real friendship stays forever. I will not forget the personnel of the mechanical engineering department because without all of you this place will not be the same. Finally, I am deeply grateful with everyone that gave me the push to achieved this goal. Thanks to all of you!!! I will take all of the good moments and never erase them from my memory!!!

I will like to acknowledge the following programs for providing funding for this research: National Nanotechnology Infrastructure Network (NNIN), Collaboration in Biomedical Engineering Research (CIBER), Laboratory Experience for Faculty at CNF, and RISE 2 BEST Program.

TABLE OF CONTENTS

ABSTRACT.....	II
ACKNOWLEDGEMENTS.....	VII
TABLE LIST.....	X
FIGURE LIST	XI
CHAPTER 1	1
1.1 MOTIVATION.....	3
1.2 LITERATURE REVIEW	4
1.3 OBJECTIVES	10
1.4 SUMMARY OF FOLLOWING CHAPTERS	11
CHAPTER 2	12
2.1 THEORETICAL BACKGROUND AND CALCULATIONS	12
2.1.1 <i>Flow Regimes</i>	12
2.1.2 <i>Navier-Stokes Equation</i>	14
2.1.3 <i>Boundary Conditions</i>	15
2.1.4 <i>Micro-Particle Image Velocimetry(PIV)</i>	18
2.1.5 <i>Stokes Number</i>	18
2.1.6 <i>Brownian Motion</i>	20
2.1.7 <i>Depth of Correlation</i>	21
2.1.8 <i>Dimensional Analysis</i>	23
CHAPTER 3	27
3.1 DESIGN AND FABRICATION OF THE MICRO-FLUIDIC DEVICE	27
3.1.1 <i>Device Design</i>	27
3.1.2 <i>Device Fabrication</i>	29
CHAPTER 4	40
4.1 DEVICE EXPERIMENTATION	40
4.1.1 <i>Device Characterization without Beads</i>	40
4.1.2 <i>Device Characterization with Beads</i>	42
4.2 MICRO-PARTICLE IMAGE VELOCIMETRY (PIV).....	43
4.3 FINITE ELEMENT ANALYSIS.....	46
CHAPTER 5	51
5.1 COMSOL MODELS COMPARISON	51
5.2 MICRO-PIV EXPERIMENTS VS. COMSOL RESULTS	54
5.3 EXPERIMENTS WITHOUT BEADS VS. COMSOL RESULTS.....	62
5.4 CHARACTERIZATION EXPERIMENTS WITH POLYSTYRENE BEADS AND COMSOL RESULTS	65
CHAPTER 6	76
6.1 CONCLUSIONS	76
6.2 FUTURE WORK.....	77

REFERENCES.....79

Table List

Tables	Page
Table 2.1: Depth of correlation for different magnifications and numerical apertures.	23
Table 4.1: Port 1 and port 2 boundary conditions for each mathematical model.	48
Table 5.1: Volumetric flow rate results of the incompressible Navier-Stokes model and the Stokes flow model.....	53
Table 5.2: Volumetric flow rate results of the incompressible Navier-Stokes model and the Stokes flow model.....	55

Figure List

Figures	Page
Figure 1.1: The particle arrives at the T-junction where a stagnation point is formed and the particle is trapped in the dock [14].	4
Figure 1.2: The image shows a cartoon of several systems for manipulation and isolation of micro-particles and biological cells [15].....	6
Figure 1.3: Particles are trapped in sequential order while the remaining particles exit the system through the main stream [10].....	7
Figure 1.4: Biological cells are trapped in small apertures along the dam that divides both channels [8].	8
Figure 1.5: Biological cells are trapped against pillars inside the flow-through chamber [8]..	8
Figure 1.6: Schematic of the serpentine device working in the forward and backward flow format [7].	9
Figure 1.7: Micro-particles trapped in sequential order in a serpentine design system [16]..	10
Figure 2.1: Reynolds number at different parts of the micro-fluidic channel with different volumetric flow rates.	14
Figure 2.2: Schematic representation of the no-slip boundary condition [19].	16
Figure 2.3: Schematic representation of the slip length boundary condition [19].....	16
Figure 2.4: Stokes number in the region of interest for different particle diameters.....	19
Figure 2.5: Brownian motion velocity error for different particle diameters.	21
Figure 2.6: Schematic of the thickness of the two dimensional plane[33].	22
Figure 3.1: Schematic of a functional linear micro-fluidic device.	29
Figure 3.2: CAD drawing of the micro-fluidic device.....	29
Figure 3.3: The fabrication process flowchart of the micro-fluidic devices.....	30
Figure 3.4: Micrograph of the micro-fluidic device.	31
Figure 3.5: Image of the pattern of a micro-fluidic device in a chrome mask.....	32
Figure 3.6: Schematic of the photolithography process.....	33
Figure 3.7: Laurell Model WS-400B-6NPP/LITE spin coater.	34
Figure 3.8: SUSS MicroTec MA-6 Mask Aligner.....	35
Figure 3.9: KLA Tencor Stylus Profiler Model P-6.	36
Figure 3.10: Schematic of the soft lithography process.....	36
Figure 3.11. Air plasma chamber (Harrik Plasma, Ithaca, NY).	38
Figure 3.12. PBS flushing of the micro-fluidic device.	39
Figure 4.1: Flowchart of the experimental approaches carried out in this project.	40
Figure 4.2: New Era Syringe Pump model NE-1000 (photo courtesy of New Era Pump Systems, Inc.).....	41
Figure 4.3: Pictures of the experimental set-up.	42
Figure 4.4: Process flow of the analysis of the experimental data from the micro-PIV.....	44

Figure 4.5: Double frame images and vector velocity field results from a micro-PIV experimental run.	45
Figure 4.6: (Left) PIV control unit (Dantec Dynamics). (Center) The 532nm Nd:YAG laser (Dantec Dynamics). (Right) An inverted microscope (Nikon Eclipse Ti-U) with a lateral camera (Dantec Dynamics).....	46
Figure 4.7: Initial COMSOL GUI to specify the module, the model and the geometry to be analyzed.	47
Figure 4.8: 3D geometry of the micro-fluidic channel in COMSOL.	47
Figure 4.9: Volumetric mesh of the 3D geometry of the micro-fluidic channel.	49
Figure 4.10: Velocity field slice plot of the studied micro-fluidic channel.	50
Figure 4.11: Pressure plot and streamlines of studied micro-fluidic channel with 20 μm sphere.	50
Figure 5.1: Case 1 (port 2 unrestricted) pressure plot using the incompressible Navier-Stokes model.....	52
Figure 5.2: Case 1 (port 2 unrestricted) pressure plot using the Stokes flow model.	53
Figure 5.3: Velocity profiles in the longitudinal direction for the incompressible Navier-Stokes model and the Stokes flow model.	54
Figure 5.4: Region of interest for the micro-PIV experiments and the cross-sectional area of the region of interest with the depth of correlation.	56
Figure 5.5: Graph of velocity profile in the longitudinal direction from the micro-PIV experiments (blue diamonds) compared to the corresponding velocity profile from the COMSOL model for case 1 (port 2 unrestricted) with 13 μm slip length at PDMS walls and no slip at glass wall (green plus sign), 20 μm slip length at all the walls (violet cross) and no slip at all the walls (red line).	56
Figure 5.6: Contour plot of the region of interest for the COMSOL model with no slip at all the walls. The centerline represents the focal plane and the other two lines represent the depth of correlation.	57
Figure 5.7: Contour plot of the region of interest for the COMSOL model with 20 μm slip length at all the walls. The centerline represents the focal plane and the other two lines represent the depth of correlation.	58
Figure 5.8: Contour plot of the region of interest for the COMSOL model with 13 μm slip length at the PDMS wall and no slip at the glass wall. The centerline represents the focal plane and the other two lines represent the depth of correlation.	59
Figure 5.9: Surface plot of the region of interest for the COMSOL model with no slip at all the walls.	60
Figure 5.10: Surface plot of the region of interest for the COMSOL model with 20 μm slip length at all the walls.	61
Figure 5.11: Surface plot of the region of interest for the COMSOL model with 13 μm slip length at the PDMS wall and no slip at the glass wall.....	61
Figure 5.12: Graph of outflow rates from experiments of characterization without beads compare to outflow rates of COMSOL model for the case 1 (port 2 unrestricted).	63

Figure 5.13: Graph of outflow rates from experiments of characterization without beads compare to outflow rates of COMSOL model for the case 2 (port 2 restricted to 25% of inflow rate).....	64
Figure 5.14: Graph of outflow rates from experiments of characterization without beads compare to outflow rates of COMSOL model for the case 3 (port 2 restricted to 50% of inflow rate).....	64
Figure 5.15: Graph of outflow rates from experiments of characterization without beads compare to outflow rates of COMSOL model for the case 4 (port 2 restricted to 75% of inflow rate).....	65
Figure 5.16: Micrograph of the experiment of the characterization with 20 μ m beads for case 1.....	66
Figure 5.17: Micrograph of the experiment of the characterization with 20 μ m beads for case 2.....	66
Figure 5.18: Micrograph of the experiment of the characterization with 20 μ m beads for case 3.....	67
Figure 5.19: Micrograph of the experiment of the characterization with 20 μ m beads for case 4.....	67
Figure 5.20: Micrograph of the experiment of the characterization with 20 μ m beads for case 5.....	68
Figure 5.21: Experimental results of characterization with 20 μ m beads for 5 different cases.	69
Figure 5.22: The region of the channel where V_{trap} and V_{channel} were measured.	70
Figure 5.23: COMSOL results of the pressure differential (ΔP) at available trap site for case 1.	71
Figure 5.24: COMSOL results of the pressure differential (ΔP) at available trap site for cases 2, 3, 4 and 5.	72
Figure 5.25: COMSOL results of the velocity ratio ($V_{\text{trap}}/V_{\text{channel}}$) at available trap site for case 1.....	73
Figure 5.26: COMSOL results of the velocity ratio ($V_{\text{trap}}/V_{\text{channel}}$) at available trap site for case 2, case 3, case 4 and case 5.	74
Figure 5.27: COMSOL results of the velocity ratio ($V_{\text{trap}}/V_{\text{channel}}$) at available trap site for case 6, case 7 and case 8.	75
Figure 5.28: COMSOL results of the pressure differential (ΔP) at available trap site for case 6, case 7 and case 8.	75
Figure 6.1: Prototype of micro-fluidic device for high-density cell isolation.	78

CHAPTER 1

In the past ten years, the scientific community has seen an increasing interest in the research of Lab-on-a-Chip devices. Lab-on-a-Chip is a device that integrates one or several laboratory functions on a single chip. The interest is due to the prospective benefits that Lab-on-a-Chip devices can offer to the fields of biological and medical sciences. Some of the benefits are the ability to manipulate large number of cells simultaneously, analysis of living single cells, miniaturization of analytical systems, minimization of reactive compounds required for analysis, and the promise of having a complete laboratory setup in small-footprint apparatus [1-3]. All of those benefits are incorporated in an experimental set-up that can be coupled with an optical system for real-time monitoring. In order to monitor the activity, the devices are made translucent to visible light for observation under transmitted or reflected light microscopy.

Polydimethylsiloxane (PDMS, Sylgard 184) has been the material of choice for biological micro-fluidic Lab-on-a-Chip applications for several reasons. PDMS is an inexpensive, flexible and optically transparent material [4]. It is also suitable for biological studies because it is permeable to certain gases but impermeable to water and is non-toxic to biological entities [4]. The PDMS is used in a fabrication process called soft lithography which is a fabrication technique that replicates structures using elastomeric stamps (see section 3.1.2 for more information). Soft lithography is an easier and less expensive fabrication method than wet bulk micromachining or ion milling. For those reasons, the

scientific community has employed PDMS soft lithography extensively for the fabrication of Lab-on-a-Chip devices.

Most Lab-on-a-Chip devices have a main purpose. Researchers have fabricated devices to perform DNA sequencing, polymerase chain reaction (PCR), electrophoresis, DNA separation, enzymatic assays, immunoassays, cell counting, cell sorting and cell culture [4-6]. The main purpose for our micro-fluidic device is to create a smart platform for the trapping and release of cells from a bulk stream using a pressure differential trapping mechanism. Some research groups have developed devices with a conceptual operation that is similar to our platform but most of them present serious limitations.

The outcome of this study should allow us to find design parameters to fabricate a densely packed system to capture hundreds or thousands of micro-scale particles (e.g. biological cells) that are suspended in a bulk solution. This densely packed design will allow the acquisition of data from multiple particles at the same time, but with the option of controlling the microenvironment of each particle individually [7]. In addition, this platform is intended to be resettable by allowing the particle removal from the trap site by reversing the flow, and reusable due to the reversible nature of the PDMS/glass bond.

This study focused on the parameter of velocity ratio (see sections 2.1.8 and 5.3 for more information) between the flow through the trap and the flow in the main channel. In order to perform this analysis, we needed to rely on mathematical models and experimental data. COMSOL was the tool of choice for the computational modeling. Experiments with a micro-particle image velocimetry (micro-PIV) and mass conservation experiments were used to validate the mathematical models. We found that by restricting the outflow at one of the

exit of the channels, we obtained different velocity ratios at the point of interest. The restriction induced was equivalent to a variation in the fluidic resistance of the channel. Various studies have demonstrated that the fluidic resistance is responsible for the distribution of the flow in the micro-fluidic channels [8-13].

1.1 Motivation

Cancer is a disease in which cells grow in an unregulated manner. These cells form malignant tumors and invade nearby organs. Cancer is a serious disease that can cause death if not treated in an early stage. Each year millions of people are diagnosed with cancer and hundreds of thousands die due to that disease. There is an evident need for tools that allow early cancer detection and treatment. Researchers have worked on devices that provide single cell isolation to study or manipulate biological cells. These devices are limited in cell entrapment capacity.

This work consists on the design, fabrication and characterization of a micro-fluidic device that will serve as a step toward high-throughput high-density cell isolation for single cell electroporation, suspended tumor cell detection, and other medical applications. The characterization of the device is crucial to develop a mathematical model and determine design parameters that will help in the design of the next generation of micro-fluidic devices. Hopefully, this next generation of micro-fluidic devices can be used to save lives with an early cancer detection system.

1.2 Literature Review

In the past decade, there has been a remarkable increase in the number of publications whose main topic is the fabrication of micro-fluidic devices for manipulation and trapping of micro-particles and biological cells. Most of the devices encountered in the literature, which focus on the hydrodynamic control of the fluid, use a physical obstruction or a pressure differential mechanism to trap and retain the micro-particles or biological cells in designated areas. In this section, some of the devices encountered in literature will be presented.

One of the first of such devices, published in 2003, used a stagnation point to isolate a single cell within a micro-channel (see Figure 1.1). The device employed the laminar flow characteristics of micro-fluidic devices to manipulate the medium flow and trap the cell at the stagnation point [14]. The stagnation point is created at the T-junction where the main stream divides into two streams [14]. Placing a dock with small drain channels at the stagnation point allows the cell to land in the dock where it gets trapped [14]. Figure 1.1 demonstrates the actual micro-fluidic device with a particle trapped inside the dock. This system is capable of trapping and retaining a particle but does not provide an easy mechanism to release the particle from the trap.

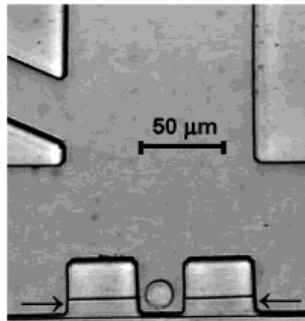


Figure 1.1: The particle arrives at the T-junction where a stagnation point is formed and the particle is trapped in the dock [14].

A 2007 review shows a schematic of multiple manipulation and trapping mechanisms for micro-particles and biological cells. Figure 1.2a presents a device where particles are hydrodynamically focused in a single file at an intersection point for interrogation [15]. Figure 1.2b is the schematic of a device that hydrodynamically transports cells to an intersection where the cells are lysed [15]. In the next micro-fluidic device, the cells are added into an aqueous solution within an immiscible fluid and transported to an interrogation point [15], as shown in figure 1.2c. In figure 1.2d and 1.2e the cells are trapped at the interrogation region using pillars or weirs [15]. Figure 1.2f shows the schematic of a device that traps cells creating a stagnation point at one of the walls of the channel [15]. Also, a system that uses filters to trap the cells at the interrogation point is presented in figure 1.2g [15]. Finally, figure 1.2h shows dielectrophoretic trap for cells [15]. The first three (a, b and c) systems presented in this review are only for manipulation of the micro-particles. This manipulation is performed by directing the particles to an interrogation point via bulk flow transport. However, in these three cases no micro-particle was trapped at a specific site. Systems d, e and g are used to trap micro-particles but none of them is designed to release the micro-particles without reversing the flow, thus, prompting the mixing of examined specimens with new specimens. The system presented in figure 1.2h uses non-mechanical means of trapping cells at specific sites but it requires high frequency electrical fields to move the cells to the trapping sites.

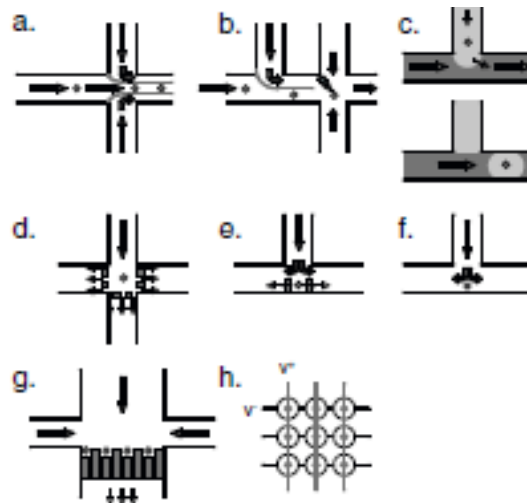


Figure 1.2: The image shows a cartoon of several systems for manipulation and isolation of micro-particles and biological cells [15].

The following micro-fluidic device was introduced in 2007 and it uses fluidic resistance to trap the particles while the bulk stream remains in its path. The micro-fluidic channel was designed as a serpentine with the traps at one wall of the serpentine connected through a small passage to the wall of the next section of the serpentine. The device can be seen in figure 1.3. This micro-fluidic device was designed to have the lowest fluidic resistance through the trap and the highest in the serpentine part of the channel [10]. Therefore, the particles are directed to the trapping site. Once the trapping site is occupied the resistance increases and the particles in the bulk stream follow the serpentine until they reach the next trapping site and the same mechanism traps the next particle. This repeats until all the trapping sites are full. This device also presents a novel but expensive particle release mechanism in which individual particles can be released to the bulk stream by the creation of a micro-bubble at the trapping site using a focused laser beam [10].

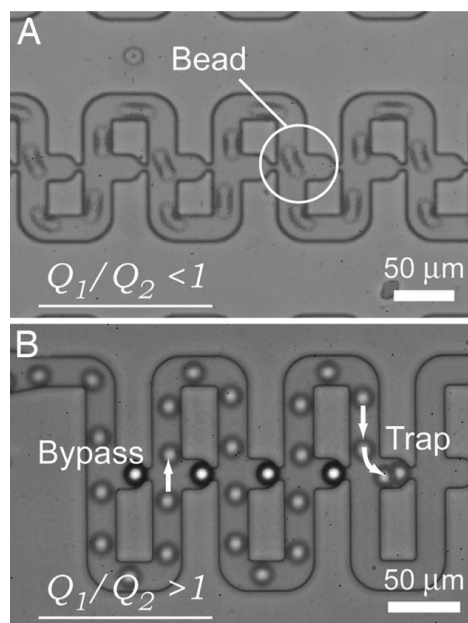


Figure 1.3: Particles are trapped in sequential order while the remaining particles exit the system through the main stream [10].

A 2009 review paper presented two other micro-fluidic devices for biological cell entrapment. The first micro-fluidic device encountered in the literature presents a two channel structure divided by a dam that has 5 μm opening along the length of the channels [8]. The main channel transports the biological cells and the other channel remains with a fluid medium [8]. Part of the main channel flow is aspirated through the opening in the dam, thus, trapping the cells [8]. One advantage of this system is that the flow can be injected through the secondary channel to release the cells to the main stream [8]. However, this system does not provide single cell isolation. The system is presented in figure 1.4.

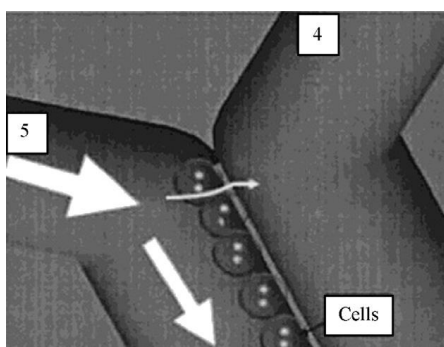


Figure 1.4: Biological cells are trapped in small apertures along the dam that divides both channels [8].

The second device uses physical obstructions as the trapping mechanism (see figure 1.5). This system consists of slanted rows of pillars with a semicircular cavity in a flow-through chamber [8]. The small cavity in the pillars was designed to trap a single cell or a small group of cells [8]. This system demonstrated that 55% of the pillars trapped a single cell, 22% trapped multiple cells and the other pillars remained empty [8]. The release of cells into the bulk stream is difficult because the cells are pinned down against a physical obstruction in the direction of the flow. This means that the flow must be reversed to release the cells, eventually, losing track of the cells that have been trapped and the remaining cells in the bulk stream.

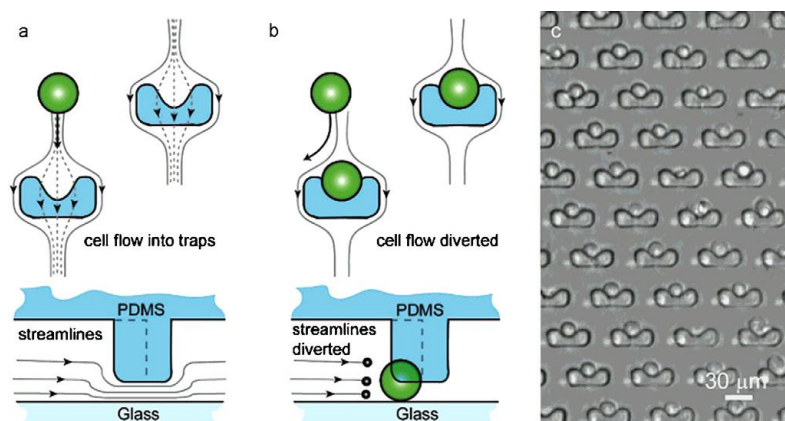


Figure 1.5: Biological cells are trapped against pillars inside the flow-through chamber [8].

A serpentine device was presented in a 2010 article which was capable of trapping and retaining biological cells using a pressure difference trapping mechanism [7]. A schematic of the device can be seen in figure 1.6. The device has a unique geometry with one inlet and one outlet that simplifies the system [7]. Also, it is resettable with the introduction of a backflow [7]. The results showed that the trapping efficiency of the device was greatly influenced with the geometry of the upper and lower channel [7]. The device had the best trapping efficiency when both channels had the same geometry [7].

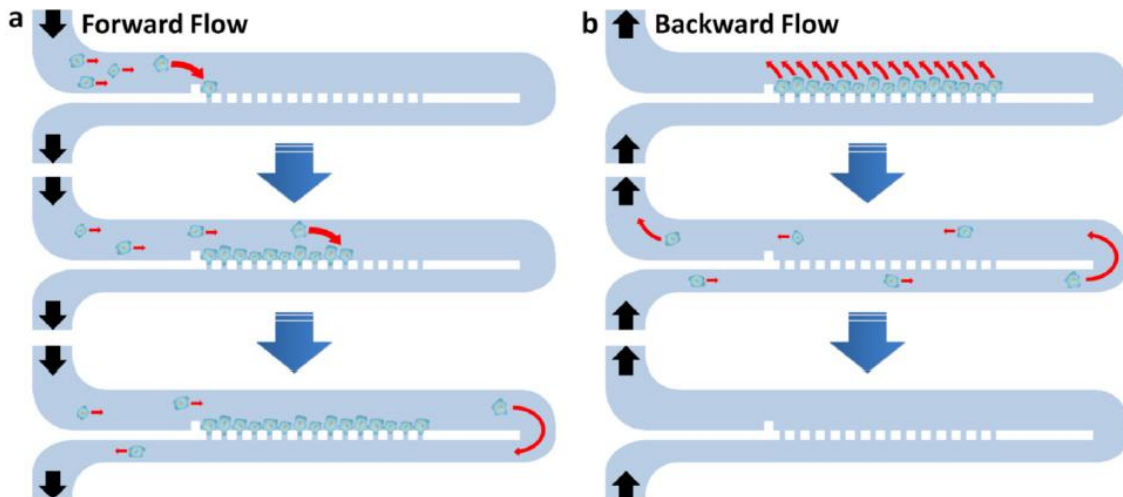


Figure 1.6: Schematic of the serpentine device working in the forward and backward flow format [7].

A sequential trapping system was presented in a 2011 paper that resembles one of the designs explored for this study. This micro-fluidic device uses a serpentine design with 20 μm traps at the smallest curvature radius of each semicircular section of the serpentine where each trapping site has a small drain channel [16]. The authors studied linear channels but reported that they had 0% of capture ratio compared with an 87.5% capture ratio with the

serpentine design [16]. The device is shown in figure 1.6. This design showed good results but due to the large spacing between traps a high-density packaging platform is unlikely.

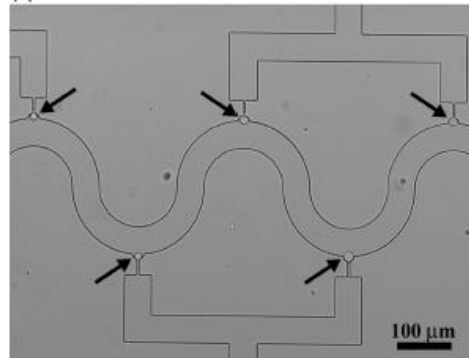


Figure 1.7: Micro-particles trapped in sequential order in a serpentine design system [16].

1.3 Objectives

The main objective of this research project was to characterize a micro-fluidic device designed to trap and retain suspended polystyrene micro-beads. The specific aims needed to achieve the main objective of the research project were the following:

- Generate and validate a mathematical model for the micro-fluidic device using COMSOL Multiphysics (commercial FEM software package).
- Identify a parameter that increases the probability of trapping 20 μm polystyrene beads.
- Find optimal operating conditions to produce single micro-particle entrapment at each trap site.

1.4 Summary of Following Chapters

Chapter 2 explains the background theory and calculation of some important parameters. The third chapter describes the design of the micro-fluidic device and the fabrication techniques used. Chapter 4 is a complete explanation of the experimental procedures and the parameters used in the finite element analysis. Results and discussion are presented in Chapter 5. The final chapter encloses the conclusion of this work.

CHAPTER 2

2.1 Theoretical Background and Calculations

2.1.1 Flow Regimes

It is always important to determine the flow regime of the fluid flow under study. Knowing the flow regime can simplify the analytical equations to be used. In order to determine the flow regime of the fluid flow it is important to explain the parameter that identifies each flow regime. The Reynolds number is a dimensionless number that represents the ratio of the inertial forces to viscous forces in a fluid and is employed to determine the dominant effect between these two forces [17-18]. The Reynolds number (Re) is an indicator of the flow regime of a fluid flow.

$$Re = \frac{\rho V D_h}{\mu} \quad (1)$$

where ρ is the fluid density, V is the fluid mean velocity, D_h is the hydraulic diameter of the channel, and μ is the dynamic viscosity of the fluid.

$$D_h = \frac{4A}{P} = \frac{4wd}{2(w+d)} = \frac{2wd}{(w+d)} \quad (2)$$

where A is the cross sectional area of the channel and P is the wetted perimeter of the channel. For a rectangular channel, D_h can be rewritten in terms of w (channel's width) and d (channel's depth).

The flow regimes can be classified into three groups laminar, transitional, and turbulent [17]. Laminar flow is a viscous dominated flow in which the fluids move in orderly sheets [17]. If the boundary conditions are steady the laminar flow is steady. The Reynolds

number maximum limit of the laminar flow regime in circular cross section channels is 2300 [17-18]. The turbulent regime is flow that is dominated by random fluid motions that are not predictable from the boundary conditions [17]. A turbulent flow is always unsteady even when the boundary conditions are steady. A flow is considered turbulent when the Reynolds number is above 4000 for a circular cross section channel [17-18]. The transitional regime of a flow has inherent instability and is an unstable flow that is not common in practice. The Reynolds number lower and upper bound for this flow regime in circular cross section channels is 2300 and 4000, respectively.

In micro-fluidic devices the Reynolds number is almost always below 1. In the device studied in this thesis, the Reynolds number varies depending on the area under study and the volumetric flow rate. Figure 2.1 shows a graph of the different possible Reynolds number in the micro-fluidic channel. As it can be seen the largest Reynolds number occurs at the smallest cross section of the channel which is the neck of the traps. It is worth mentioning that the volumetric flow rate used in the experiments is $50\mu\text{L/hr}$ which yields a Reynolds number minor to 1 in any part of the channel. This is extremely important because if the Reynolds number is less than 1 the Stokes flow approximation can be use. Using the Stokes flow approximation simplifies the analysis consuming less computational resources for the finite element analysis model.

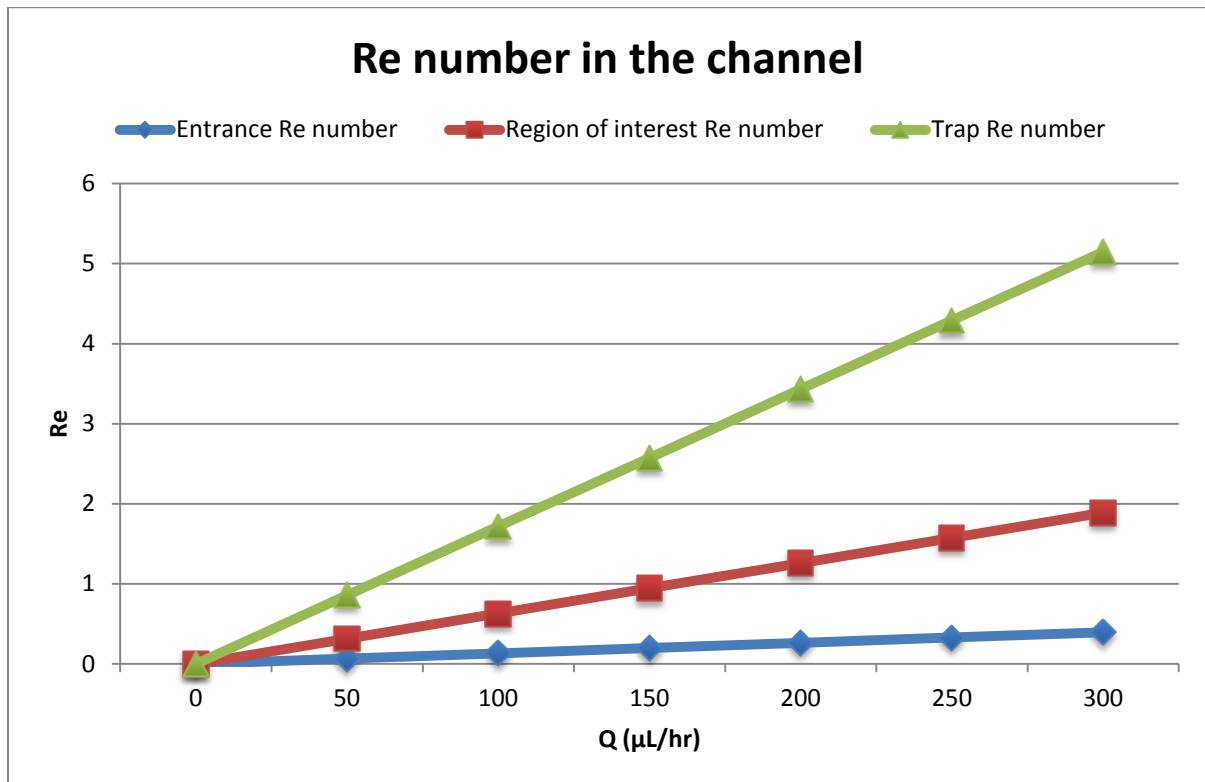


Figure 2.1: Reynolds number at different parts of the micro-fluidic channel with different volumetric flow rates.

2.1.2 Navier-Stokes Equation

The Navier-Stokes equations are used to describe the motion of a Newtonian fluid [17-18]. The Navier-Stokes equations can be simplified depending on many conditions. The first simplification that can be made to the Navier-Stokes equations is the incompressible flow assumption. The following equation results from that assumption.

$$\rho \frac{\partial \vec{u}}{\partial t} + \rho \vec{u} \cdot \nabla \vec{u} = -\nabla p + \mu \nabla^2 \vec{u} \quad (3)$$

where ρ is the fluid density, p is pressure, μ is the dynamic viscosity of the fluid, and \vec{u} is the fluid velocity vector. The left part of the equation contains the inertial terms and the right

side contains the divergence of stress terms. The first term of the left part of the equation is the unsteady acceleration term and the second term is the convective acceleration term. The first term of the right side of the equation is the pressure gradient and the second term is the viscosity term.

There are cases in which the inertial terms of the Navier-Stokes equation can be neglected and the equation reduces to the Stokes equation. If the equation is rewritten in a nondimensional form it can be seen how a small Reynolds number simplifies the Navier-Stokes equation.

$$Re \frac{\partial \vec{u}^*}{\partial t^*} + Re \vec{u}^* \cdot \nabla^* \vec{u}^* = -\nabla^* p^* + \nabla^{*2} \vec{u}^* \quad (4)$$

If $Re \ll 1$, then the unsteady and convective terms can be neglected yielding the following equation.

$$\nabla p = \mu \nabla^2 \vec{u} \quad (5)$$

A rule of thumb to consider this a good approximation is that the $Re < 0.1$ [17]. This equation is much simpler to solve than the Navier-Stokes equation because both the velocity and pressure terms are linear.

2.1.3 Boundary Conditions

Commonly, there are two types of boundary conditions that describe the liquid-solid behavior at geometrical boundaries. One is the no-slip boundary condition and the other is partial slip or slip length boundary condition.

No slip boundary condition is the most accepted boundary condition. The no slip condition states that at a solid boundary, the fluid will have zero velocity relative to the boundary [19]. Figure 2.2 shows a schematic of the no slip boundary condition.

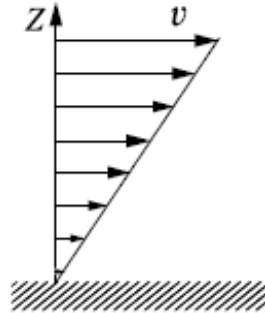


Figure 2.2: Schematic representation of the no-slip boundary condition [19].

Contrary to the no slip condition the slip length boundary condition states that the relative velocity between the fluid and the boundary is not zero [19]. The term of slip length, b , is the distance between the fluid velocity at the boundary and the zero velocity if the velocity profile is extended beyond the boundary [19]. Figure 2.3 illustrates the slip length boundary condition.

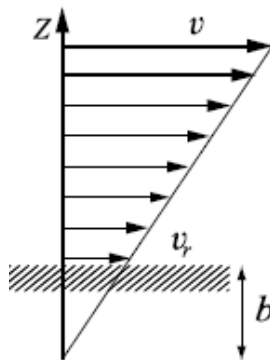


Figure 2.3: Schematic representation of the slip length boundary condition [19].

There are many possible causes for a slip condition at the boundary. Some of these conditions are:

- Surface wettability: Liquids are more likely to slip on poorly wetted surfaces. A high contact angle is indicative of a weak interaction between liquid and solid causing the fluid molecules to slide across the solid creating slip conditions [19-21].
- Surface roughness: Boundary slip is also linked to surface roughness, particularly to corner flow. Corner flows are flows that occur in surfaces with high curvature. Corner flows are responsible for slip conditions in channels [19, 22-23].
- Nanobubbles or gaseous films: Several authors believe that the presence of small amounts of gas trapped on rough and/or hydrophobic surfaces can create an apparent slip. The apparent slip length then provides a means to average the flow over a heterogeneous surface, where regions of perfect slip exist over the nanobubbles and no-slip on the surface [19, 24-28].
- Adsorption of species from solution: Slip has also been shown to be simply enhanced when surfactants are adsorbed on the surface [19, 29-30].
- Curvature: A few publications have highlighted that the curvature of the solid boundary may also affect dramatically the liquid slip behavior [19, 31].
- Viscosity: Apparent slip could arise in a thin stratum of liquid of lower viscosity formed next to the wall of a smooth solid surface. This is thought to occur for highly hydrophobic surfaces [19, 32].

2.1.4 Micro-Particle Image Velocimetry(PIV)

Particle Image Velocimetry (PIV) is used in microscale systems to visualize fluid flow [17]. The PIV procedure is: First, a fluid flow is seeded with particulate fluid tracers, most of the time the particles are fluorescent polystyrene beads. Then two images of the fluid tracers are rapidly recorded. The setup usually involves mating a dual-pulse laser to a microscope and recording the fluorescence from the beads with a charge-coupled device (CCD) camera. Finally, the two images are correlated (see section 4.2 for more information about PIV) [17, 33]. There three important parameters to determine the size of the particles to be used. The Stokes number determines the particle lag time and this number has to be minimized. The Brownian motion error which is random movement of the particles and this error can be minimized by selecting larger particles. The depth of correlation which indicates the distance from the focal plane at which particles contribute to the image correlation. This last parameter also increases the errors in measurements but it is limited to the equipment. All of these parameters will be explained in the next sections and a brief analysis to determine the particle size will be demonstrated.

2.1.5 Stokes Number

An important parameter to verify if the particles are in a steady state within the local velocity field is the Stokes number. The Stokes number is the ratio of the particle lag time to the characteristic time over which the flow changes [17, 33-34]. If the Stokes number is much smaller than 1 then it can be assumed that the particles travel at a similar velocity as the fluid flow. Since we are using fluorescent particles to study the flow with a PIV tool, the

Stokes number for the seed particles has to be less than 1 in order for the micro-PIV results to be valid.

$$Sk = \frac{2a\rho_p U_p}{9\mu} \quad (6)$$

where a is the radius of the sphere, ρ_p is the density of the sphere, U_p is the velocity of the particle and μ is the dynamic viscosity of the fluid.

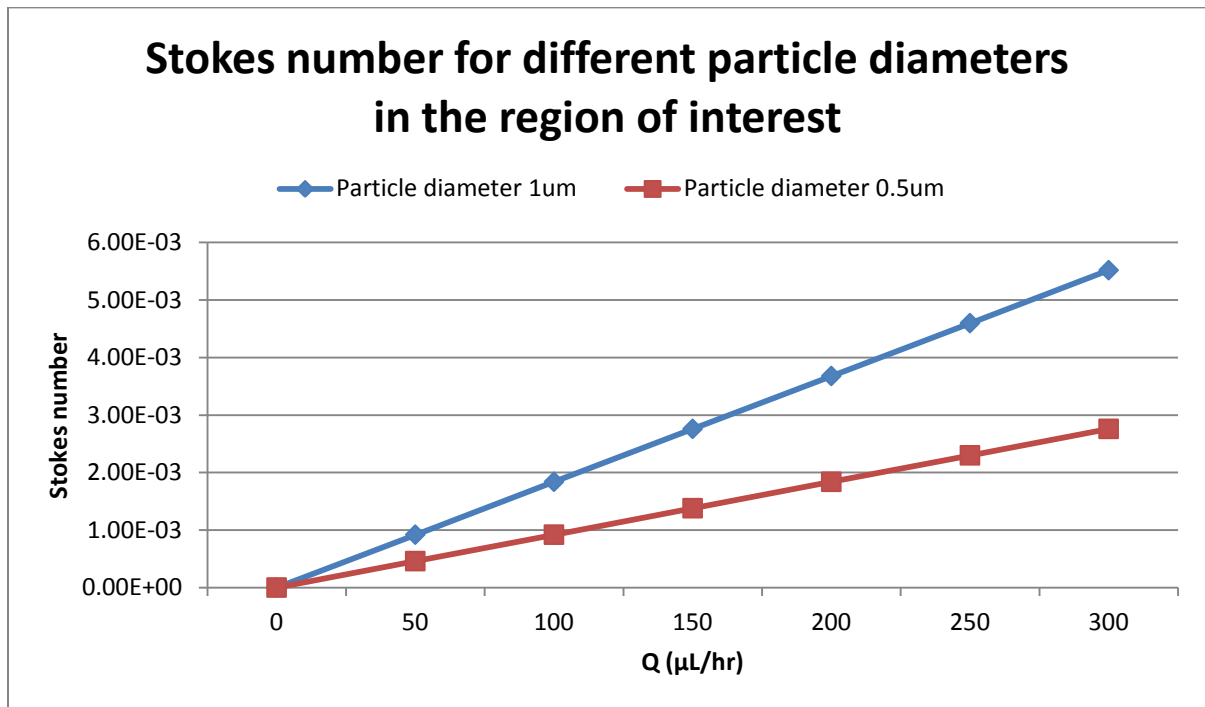


Figure 2.4: Stokes number in the region of interest for different particle diameters.

Figure 2.4 demonstrates the variation of the Stokes number for two different particle diameters. As it is shown, the Stokes number is smaller for the particle of 0.5 μm in diameter, but both are well under unity ($Sk \ll 1$). It follows that both particles satisfy the criterion and can be used to study our micro channel flows with the PIV technique. The particle of 1 μm

presents the advantage that since it is larger it reduces the error due to Brownian motion, which discussed in the next section.

2.1.6 *Brownian Motion*

Brownian motion is the random motion of particles due to the stochastic nature of fluid forces under certain conditions [17, 33, 35]. This motion is more important when the particle size decreases because individual particle-fluid collision becomes larger. The Brownian motion is related to the particle diffusivity D :

$$\langle \Delta u \rangle^2 = \frac{2D}{\Delta t} \quad (7)$$

Where D is particle diffusivity and Δt is time between exposures. The diffusivity of the particle is defined as:

$$D = \frac{k_b T}{6\pi\mu a} \quad (8)$$

where k_b is Boltzmann's constant, T is the temperature, a is the radius of the particle and μ is the dynamic viscosity of the fluid.

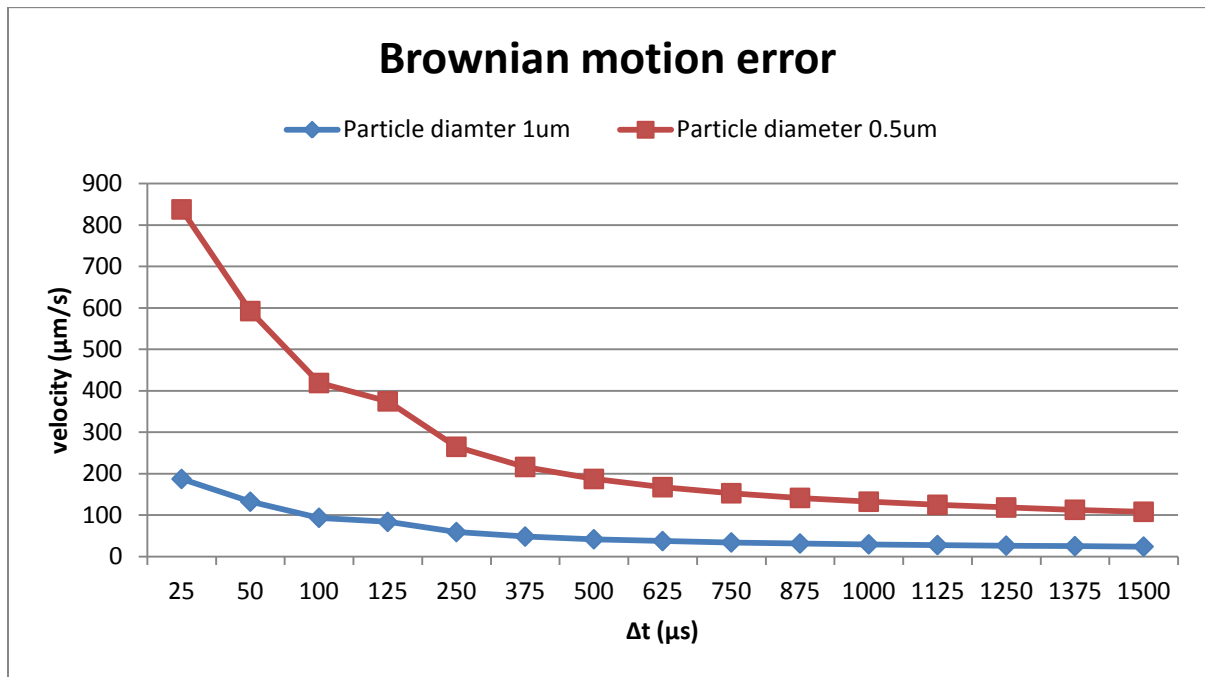


Figure 2.5: Brownian motion velocity error for different particle diameters.

The previous graph (figure 2.5) shows the Brownian motion error for both particle sizes. It is appreciable that the error is greatly reduced using the particle of 1 μm especially for small time between exposures. The particle selected for the micro-PIV analysis was the 1 μm diameter particle because it reduces the Brownian motion error and it is below the Stokes criterion.

2.1.7 Depth of Correlation

The two-dimensional measurement plane has a thickness that is determined by the depth of field of the objective lens and the seed particle properties [33, 36]. This thickness of the measurement volume is an important experimental parameter in μPIV and it is referred to as the depth of correlation [33]. The depth of correlation is the depth where the seed particles

still contribute usable information for the image acquisition system, even if they are not in the focal plane. Figure 2.6 shows the schematic of the thickness of the two dimensional plane. The equation commonly accepted to determine the depth of correlation is shown below.

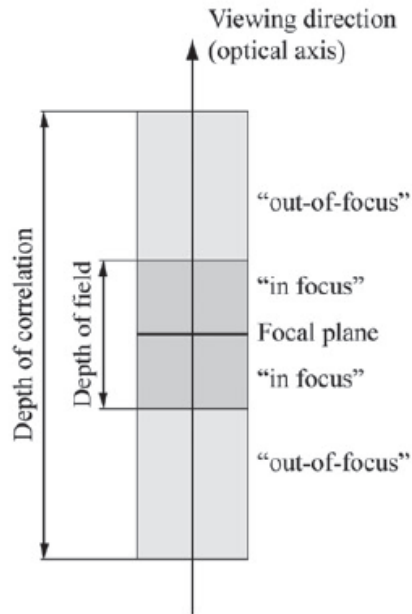


Figure 2.6: Schematic of the thickness of the two dimensional plane[33].

$$\delta_{DOC} = 2 \left[\frac{(1-\sqrt{\varepsilon})}{\sqrt{\varepsilon}} \left(\frac{n_0^2 d_p^2}{4NA^2} + \frac{5.95(M+1)^2 \lambda^2 n_0^4}{16M^2 NA^4} \right) \right]^{\frac{1}{2}} \quad (9)$$

where d_p is the particle diameter, λ the light wavelength, M the image magnification, n_0 is the refractive index of the lens immersion fluid (air in our case), NA is the numerical aperture of the lens and ε is the relative threshold below which the defocused particle images no longer contribute significantly to the displacement-correlation peak, normally set to be equal to 0.01

The results of this analysis are shown in table 2.1 for different magnification and numerical apertures used in experimentation. As it can be see there can be an error in measurement due to the contribution of out of focus particles. These particles can be at a distance as small as 1.8 μm or as large as 6 μm from the focal plane. The larger the depth of correlation, the larger the possible error in the measurements of the PIV.

Table 2.1: Depth of correlation for different magnifications and numerical apertures.

Particle diameter (μm)	1	1	0.5	0.5
Magnification	20x	40x	20x	40x
Numerical aperture	0.45	0.6	0.45	0.6
Depth of correlation (μm)	12.10	5.75	10.63	3.78

2.1.8 Dimensional Analysis

Dimensional analysis is an important tool that allows researchers to determine important parameters that govern the behavior of a fluidic system without the need for experimentation. This method uses non-dimensional combinations of system variables to determine the important parameters that control the fluidic system [18]. The following steps are a methodological procedure that helps to determine the non-dimensional (π) terms [18].

1. List all the variables that are involved in the problem.
2. Express each of the variables in terms of basic dimensions
3. Determine the required number of Π terms
4. Select a number of repeating variables, where the number required is equal to the number of reference dimensions

5. Form a Π term by multiplying one of the non-repeating variables by the product of the repeating variables, each raised to an exponent that will make the combination dimensionless.
6. Repeat step 5 for each of the remaining non-repeating variables.
7. Check all the resulting Π terms to make sure they are dimensionless.
8. Express the final form as a relationship among the Π terms, and think about what it means.

Now that the steps to produce the dimensional analysis have been mentioned we can find the Π terms that define the system.

$$F_{bead} = f(D, \rho, \mu, V_{channel}, V_{trap}) \quad (10)$$

1. Dimensional parameters

$$F_{bead}, D, \rho, \mu, V_{channel}, V_{trap} \quad n = 6$$

2. Primary dimensions

$$M, L, t \quad r = 3$$

$$F = \frac{ML}{t^2} \quad (11)$$

$$D = L \quad (12)$$

$$\rho = \frac{M}{L^3} \quad (13)$$

$$\mu = \frac{M}{Lt} \quad (14)$$

$$V_{channel} = \frac{L}{t} \quad (15)$$

$$V_{trap} = \frac{L}{t} \quad (16)$$

3. Require number of Π terms

$$\Pi = n - r = 6 - 3 = 3 \quad (17)$$

4. Repeating variables

$$\rho, D, V_{trap}$$

5. The Π terms

$$\Pi_1 = \rho^a V_{trap}^b D^c F = \left[\frac{M}{L^3} \right]^a \left[\frac{L}{t} \right]^b [L]^c \left[\frac{ML}{t^2} \right] = M^0 L^0 t^0 \quad (18)$$

$$M: a + 1 = 0 \therefore a = -1 \quad (19)$$

$$t: -b - 2 = 0 \therefore b = -2 \quad (20)$$

$$L: -3a + b + c + 1 = 0 \therefore c = -1 + 3a - b = -2 \quad (21)$$

$$\Pi_1 = \frac{F}{\rho V_{trap}^2 D^2} \quad (22)$$

$$\Pi_2 = \rho^a V_{trap}^b D^c \mu = \left[\frac{M}{L^3} \right]^a \left[\frac{L}{t} \right]^b [L]^c \left[\frac{M}{Lt} \right] = M^0 L^0 t^0 \quad (23)$$

$$M: a + 1 = 0 \therefore a = -1 \quad (24)$$

$$t: -b - 1 = 0 \therefore b = -1 \quad (25)$$

$$L: -3a + b + c - 1 = 0 \therefore c = 1 + 3a - b = -1 \quad (26)$$

$$\Pi_2 = \frac{\mu}{\rho V_{trap} D} \quad (27)$$

$$\Pi_3 = \rho^a V_{trap}^b D^c V_{channel} = \left[\frac{M}{L^3} \right]^a \left[\frac{L}{t} \right]^b [L]^c \left[\frac{L}{t} \right] = M^0 L^0 t^0 \quad (28)$$

$$M: a = 0 \therefore a = 0 \quad (29)$$

$$t: -b - 1 = 0 \therefore b = -1 \quad (30)$$

$$L: -3a + b + c + 1 = 0 \therefore c = -1 + 3a - b = 0 \quad (31)$$

$$\Pi_3 = \frac{V_{channel}}{V_{trap}} \quad (32)$$

The second Π term obtained is the inverse of the Reynolds number and the last Π term is the inverse of the velocity ratio (which will be define later) that is part of the analysis of this thesis. It will be proven in chapter 5 that the velocity ratio plays an important role to predict if a bead will be trap in the micro-fluidic device.

CHAPTER 3

In this section a detailed description of the fabrication process of the device will be presented. This description comprehends the design of the micro-fluidic device, the fabrication of the chrome mask, SU-8 mold and the PDMS-glass device. The surface modification of the micro-fluidic channel is also explained.

3.1 Design and fabrication of the micro-fluidic device

3.1.1 Device Design

The purpose of this section is to determine all of the required parameters to fabricate a micro-fluidic device that works successfully. As stated before, the main goal of the micro-fluidic devices is to capture and retain micron sized particles (e.g. biological cells, polystyrene micro-beads) in isolated sites, but still have the option to easily release the particles to the main stream. Figure 3.1 is a schematic of the micro-fluidic device. This device is intended for biological applications but during the characterization process polystyrene micro-particles were used to mimic biological cells movement when suspended in a fluid medium. Using non-living particles facilitated the experimental process. It can be found in literature that polystyrene beads are the micro-particle of choice for experimenting with micro-fluidic devices. The particles are a good model to mimic movement behavior but not physical changes of the biological cells because the polystyrene particles are rigid compared to living cells.

The device was designed based on the fact that the fluid flow in the channel will be a laminar flow due to its low Reynolds number ($Re < 1$). This low Re states that the fluid flow is

dominated by the viscous forces and the fluid moves in orderly sheets. This means that the particle that is trap in the path of these sheets will remain in that path or streamline. If the particle is moving in a streamline near the traps it will be trapped if the streamline is completely diverted to the trap due to the mass ratio (related to the velocity ratio) between the fluid of the upper channel and the fluid through the trap. Also, the device has small obstruction in the upper wall of the upper channel to divert the flow near the traps. If the path of the particle is not completely diverted to the traps the particle will exit the device through the upper channel. This provides space for other particles to be trap without particle agglomeration in the device. The device operation is explained next.

The suspended beads enter the device through port 1. The lower channel is filled with the same medium used to suspend the beads. Port 3 and 4 remain under atmospheric pressure. The upper and lower channels are linked by 3 μm apertures at the trapping sites. A pressure difference is created between both channels. As the micro particle (polystyrene beads with 20 μm in diameter were used in this study) flow through the upper channel, this pressure difference redirects the closest bead to a 25 μm semicircular cavity that is in the upper part of the 3 μm apertures. The beads will be trapped at each isolated site (as illustrated in the figure with the dark blue circles) and once all the sites are occupied the remaining beads in the main stream will exit the device through port 2 (as illustrated with the light blue circles). The pressure difference will keep the beads in the trapping sites. If a flow with no beads is entered through ports 3 and 4 the beads will be removed from the trapping sites into the main stream and exit the device through port 2. The upper and lower channels illustrated in the figure have a width of 60 μm to prevent cell cluttering and the out-of-plane dimension

(height) of the device is $30\ \mu\text{m}$. Figure 3.2 illustrates the most important dimensions of the area of interest of the micro-fluidic device.

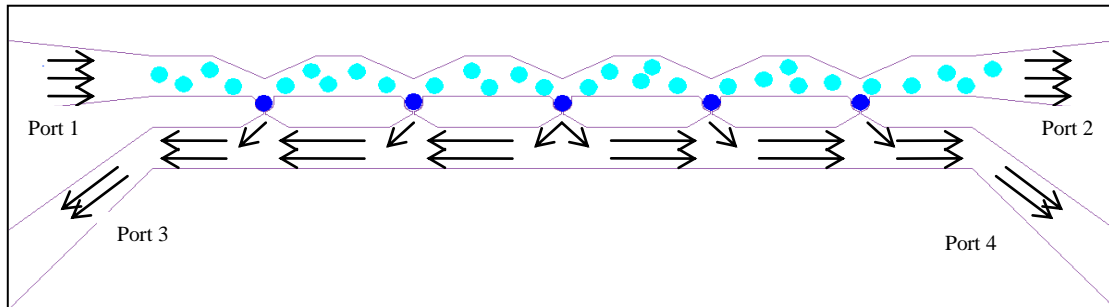


Figure 3.1: Schematic of a functional linear micro-fluidic device.

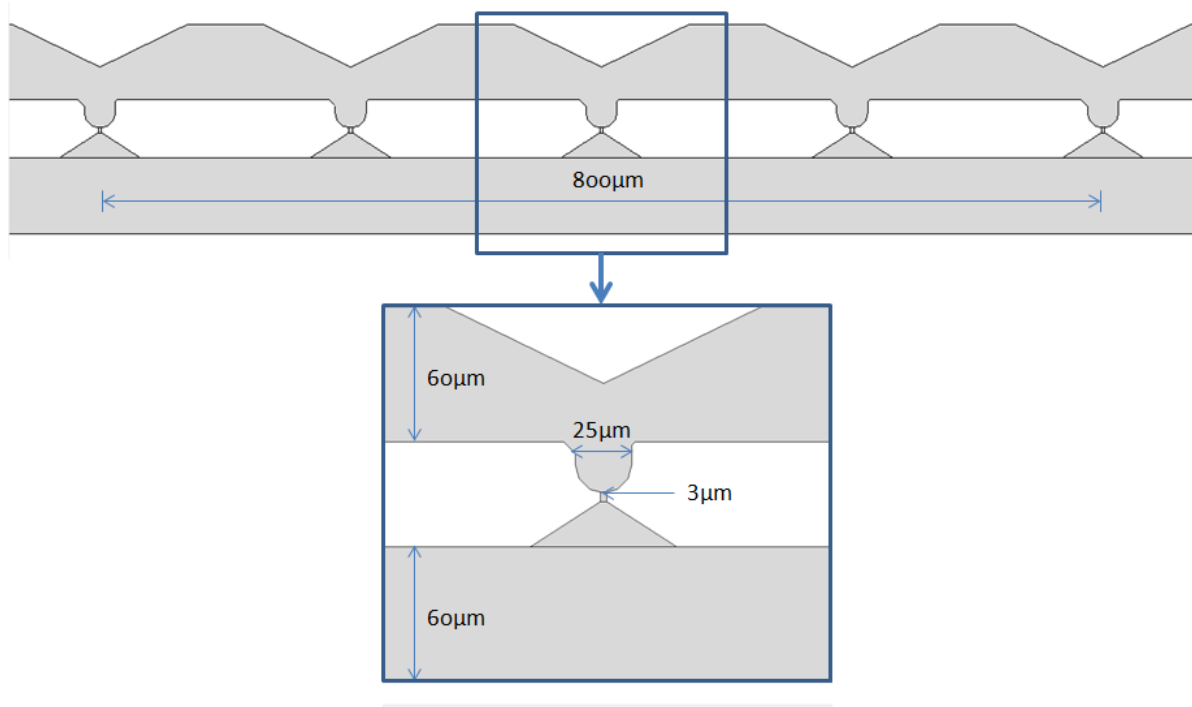


Figure 3.2: CAD drawing of the micro-fluidic device.

3.1.2 Device Fabrication

Once the preliminary design of the device was obtained, the fabrication process was initiated. The fabrication flowchart of the micro-fluidic device is shown in figure 3.3. The

micro-fluidic device was fabricated using soft lithography and consists of parallel canals that are linked by small apertures that function as localized pressure-gradient traps. Figure 3.4 shows an image of a micro-fluidic device.

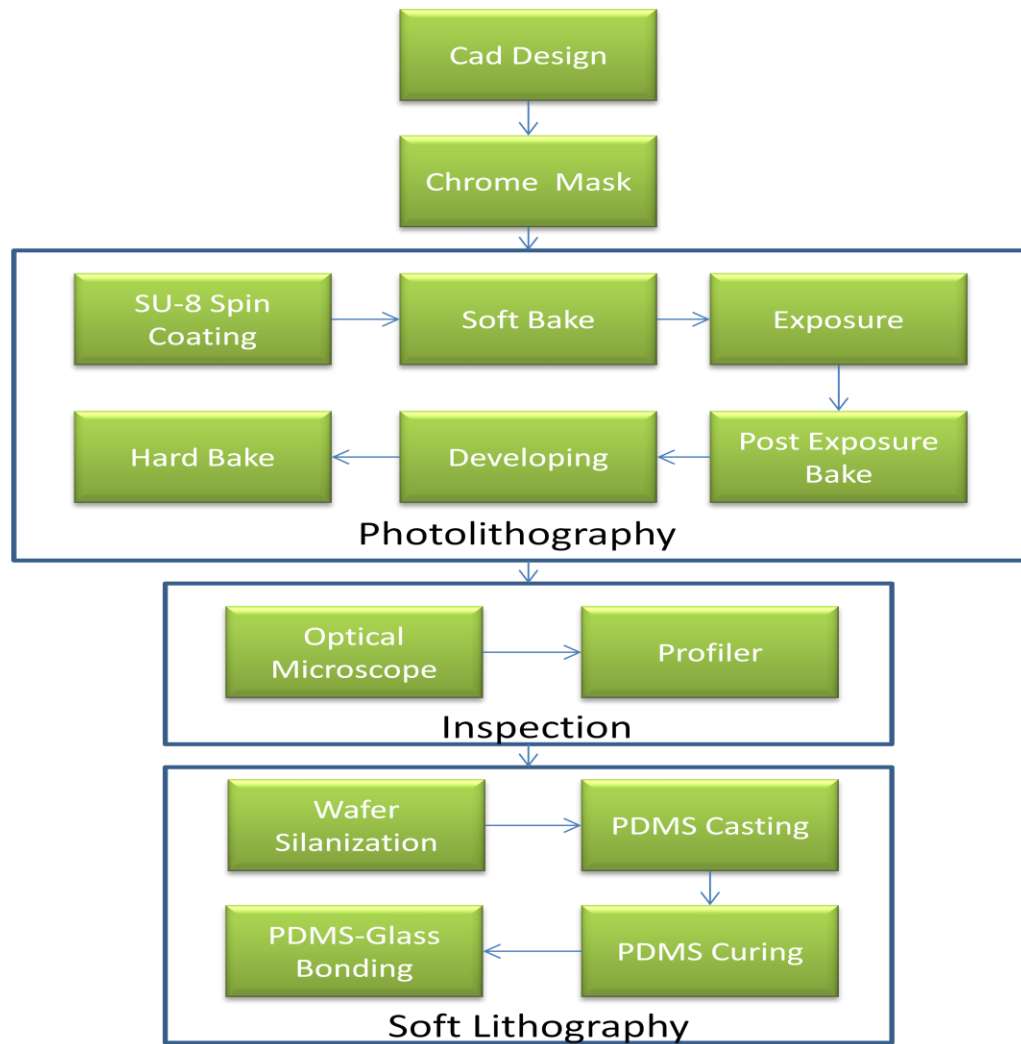


Figure 3.3: The fabrication process flowchart of the micro-fluidic devices.

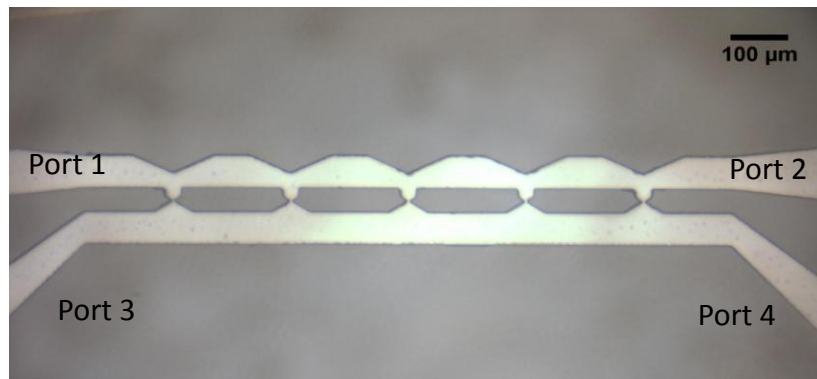


Figure 3.4: Micrograph of the micro-fluidic device.

The first step in the fabrication process was to draw the proposed micro-fluidic device using CAD software. This drawing was used to fabricate the chrome masks for the photolithography procedure. Most commercially available CAD softwares are useful, but the most commonly used for the design of MEMS and micro-fluidics are Tanner L-Edit and AutoCAD. The CAD file obtained was used to fabricate the chrome masks. The fabrication of the chrome mask consists in writing a pattern with a laser (Heidelberg Mask Writer DWL2000, Cornell Nanoscale Science and Technology Facility) onto a square fused quartz substrate covered with chrome and photoresist. The photoresist was exposed by the laser into the desired shape and was used as a mask for the chrome etching step. Once the exposed photoresist was developed, the exposed chrome was etched away and the pattern drawn in the CAD software was transferred to the chrome. The function of the chrome was to avoid ultraviolet light to pass through the quartz substrate during the photolithography process. Therefore, etching the pattern in the chrome allows for the transfer of the micro-fluidic device pattern to a photo-sensitive material in the photolithography process with remarkable resolution. Figure 3.5 shows an image of a mask employed in the fabrication of the micro-fluidic devices.

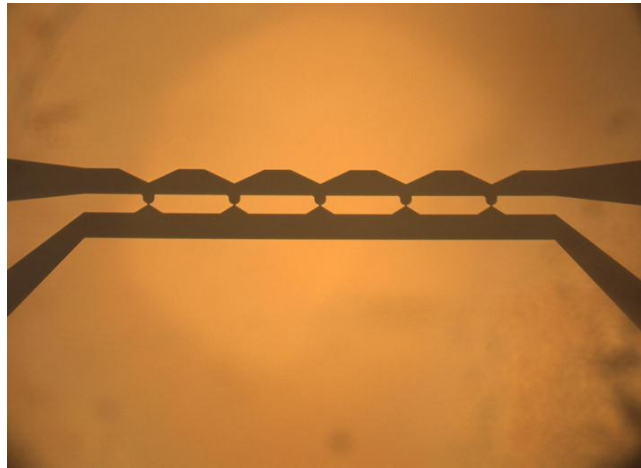


Figure 3.5: Image of the pattern of a micro-fluidic device in a chrome mask.

Photolithography is a process used in micro-fabrication to remove parts of a thin film. It uses ultraviolet light to transfer patterns from the chrome mask to a photo-sensitive material on the substrate. Usually, the size of the features of the patterns is in the micrometer scale and to avoid any damage during the transfer of the pattern to the photoresist this process is performed in a clean environment. Therefore, the photolithography process is carried out in a room where the size and the quantity of the particles in the air can be controlled. For the fabrication of our devices, we used the Class 100 (ISO Class 5) cleanroom available at the Micro and Nanoscale Devices Research Laboratory in UPRM. Also, the wavelength of the illumination is controlled to avoid undesired exposure of the photoresist. Figure 3.6 is a schematic of the photolithography process for the fabrication of the device.

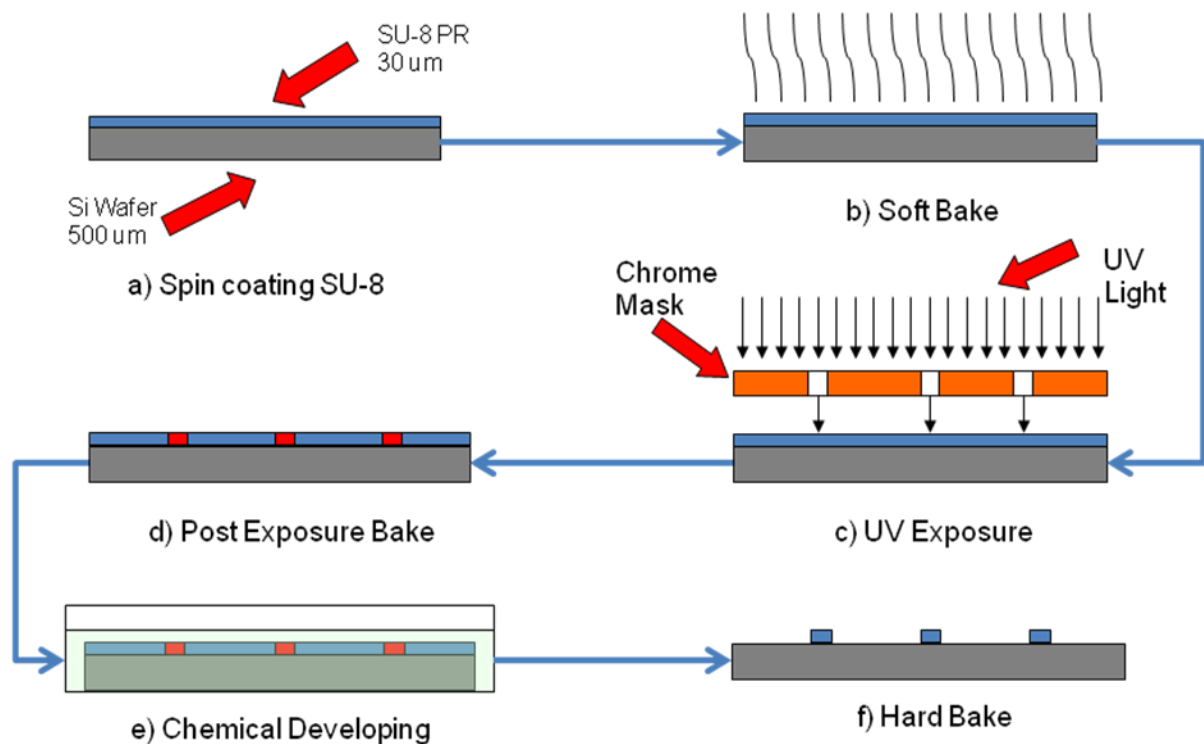


Figure 3.6: Schematic of the photolithography process.

The photo-sensitive material used is SU-8 which is an epoxy-based negative photoresist. It is photo-sensitive in the ultraviolet light range (UVA, 400nm - 315nm wavelength). It is commonly used in the fabrication of molds for soft lithography. An SU-8 thin film of approximately 30 μm was necessary to fabricate the SU-8 mold. In order to obtain such a thickness, a spin coater was required. First, SU-8 was deposited on top of a clean silicon substrate by pouring it directly from the bottle. Then the resist was evenly distributed over the surface of the substrate by rotating the substrate at high rotational speed with a spin coater. The spin coating parameters were divided in two steps. In the first step, the substrate rotated for 10 seconds at 500 rpm with an acceleration of 110 rpm/sec. In the second step, the substrate rotated for 60 seconds at 1000 rpm with an acceleration of 330

rpm/sec. The spin coater used was a Laurell Model WS-400B-6NPP/LITE at the Micro and Nanoscale Devices Research Laboratory in UPRM.



Figure 3.7: Laurell Model WS-400B-6NPP/LITE spin coater.

The SU-8 was then soft baked to eliminate the excess of solvent and harden the SU-8 thin film. This soft bake was a two step process. The first step was at a temperature of 65 °C for 1 minute and the second step was carried out at 95 °C for 7 minutes.

The SU-8 is a negative photo-sensitive resin which means that the SU-8 that is exposed to ultra-violet light (UVA, 400nm-315 nm wavelength) becomes insoluble. This property of the photo-sensitive resin makes possible the fabrication of devices with features in the micro-scale. To expose the SU-8 to ultra-violet light a mask aligner was needed. The function of the mask aligner is to align and create contact between the chrome mask and the substrate with the SU-8. The chrome mask was placed in direct contact with the wafer coated with SU-8 to have a near perfect pattern transfer from the mask to the photoresist. The other parameter was the exposure time which was 19.5 seconds. The mask aligner used was a SUSS MicroTec MA-6 at the Micro and Nanoscale Devices Research Laboratory in UPRM.



Figure 3.8: SUSS MicroTec MA-6 Mask Aligner.

A post exposure bake was performed to harden the exposed SU-8. The parameters of the post exposure bake were the same as the parameters for the soft bake. The soluble SU-8 was removed with a chemical agent in a process called developing. The substrate was submerged in SU-8 developer until the patterns were well defined. Afterwards the substrate was rinsed with isopropyl alcohol, to stop the developing process, followed by distilled water. Hard bake was a heating process performed after the developing to solidify and extend the life of the SU-8 pattern on the silicon (Si) substrate. The process was carried out at 175 °C for 15 minutes. An Olympus BX-41 reflected light microscope was used to verify the integrity of the SU-8 patterns and the size of the critical features of the pattern.

A profilometer (shown in figure 3.9) was used to measure the height of the SU-8 thin film. Measurements were taken at multiple parts of the SU-8 patterns to verify that the height was uniform. The height of the SU-8 pattern was found to be between 28 μm and 30 μm .



Figure 3.9: KLA Tencor Stylus Profiler Model P-6.

The previous fabrication process only describes the fabrication of the SU-8 mold. The soft lithography process consists in the transfer of the structures on the SU-8 mold to a Polydimethylsiloxane (PDMS, Sylgard 184) film. A schematic of the process is shown in figure 3.10. The PDMS is a liquid polymer that hardens once it is mixed with a curing agent and this allows transferring of the SU-8 pattern to the PDMS while it hardens.

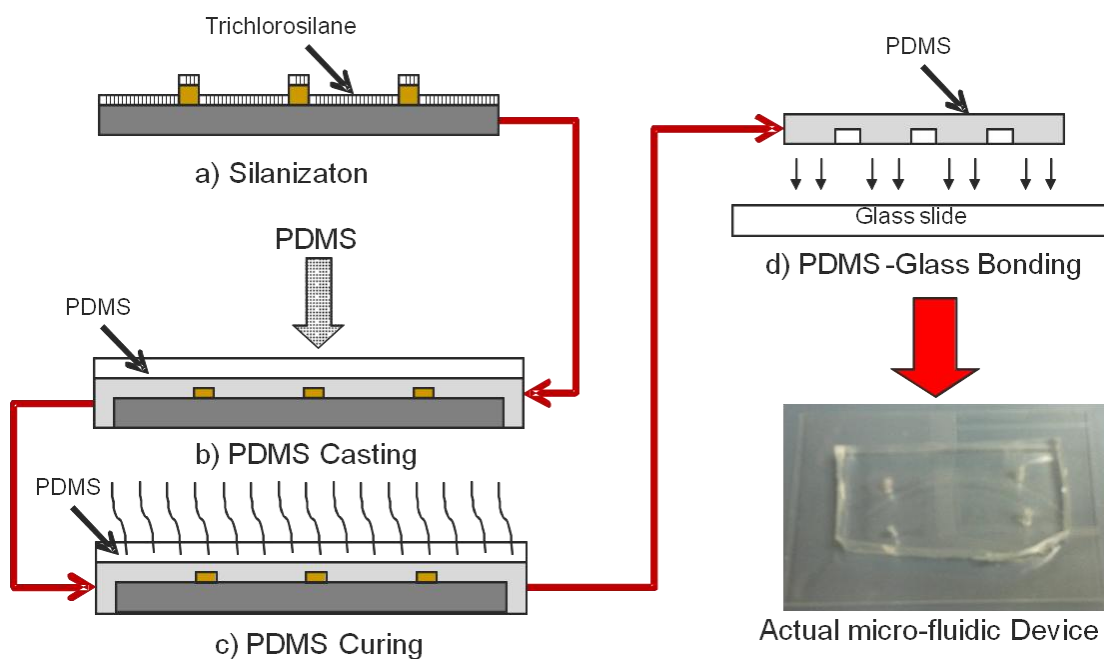


Figure 3.10: Schematic of the soft lithography process.

The first step in the soft lithography process was the silanization of the SU-8 mold and the purpose was to avoid the adhesion between the PDMS and the SU-8 mold during the PDMS casting. The process consisted of the deposition of a thin film of Trichlorosilane (HCl_3Si) in vacuum environment. The deposition time was 1 hour.

The second step was the PDMS casting and curing. The PDMS consist of two chemical agents, the PDMS elastomer and the PDMS curing agent, which are both in liquid state. To create a PDMS film with thickness of approximately 5 mm, a total of 100 grams of both chemical agents was needed. The ratio was 10 parts of PDMS elastomer (90.9g) and 1 part PDMS curing agent (9.1g). The components were mixed until a white paste was attained. This solution contained bubbles that were removed by a process known as degassing. The degassing process consisted of placing the solution in a vacuum environment. Then the PDMS solution was poured on top of the SU-8 mold and cured on a hot plate at 65 °C for 4 hours. Once cured, the PDMS was peeled off from the SU-8 mold. The opening ports were fabricated with a biopsy punch.

Before experimentation the micro-fluidic device had to be thoroughly cleaned and the PDMS glass surfaces had to be functionalized with bovine serum albumin (BSA). The BSA main purpose is to avoid cell adhesion to the walls of the channel as suggested by previous experiments [37-39]. The PDMS film and the glass slide were cleaned by gently rubbing a 5% solution of Contrad 70. Both pieces were rinsed with distilled water for approximately 1 minute to remove the solution and particles from the surfaces. The PDMS and the glass slide were sprayed with compressed nitrogen to remove the distilled water from the surfaces. Once

cleaned, the PDMS and the glass slide were reversibly bonded enclosing the micro-pattern in the PDMS. Air Plasma was used to briefly convert the hydrophobic surfaces of the PDMS and the glass to hydrophilic surfaces for ease of introduction of the BSA through the channel. The assembled micro-fluidic device was placed in an air plasma chamber (Harrick Plasma) for 10 minutes at the highest plasma intensity. The plasma chamber is shown in figure 3.11. The micro-fluidic device was extracted from the air plasma chamber and BSA was injected through one port. The hydrophilic property at the surfaces of the PDMS and the glass helped to rapidly distribute the BSA through the micro-fluidic channel. The device was allowed to rest for at least 2 hours in a refrigerated environment to avoid evaporation. Flexible tubing was added to connect the device with the syringes. All micro-fluidic devices were flushed with PBS just before experimentation to extract the BSA. Figure 3.12 shows how the micro-fluidic channels were flushed with PBS.



Figure 3.11. Air plasma chamber (Harrick Plasma, Ithaca, NY).



Figure 3.122. PBS flushing of the micro-fluidic device.

CHAPTER 4

4.1 Device Experimentation

This section is dedicated to the description of the experimental procedures and mathematical analysis used for the characterization and study of the micro-fluidic devices. The flowchart in figure 4.1 shows the different experiments and mathematical analysis proposed in this research project.

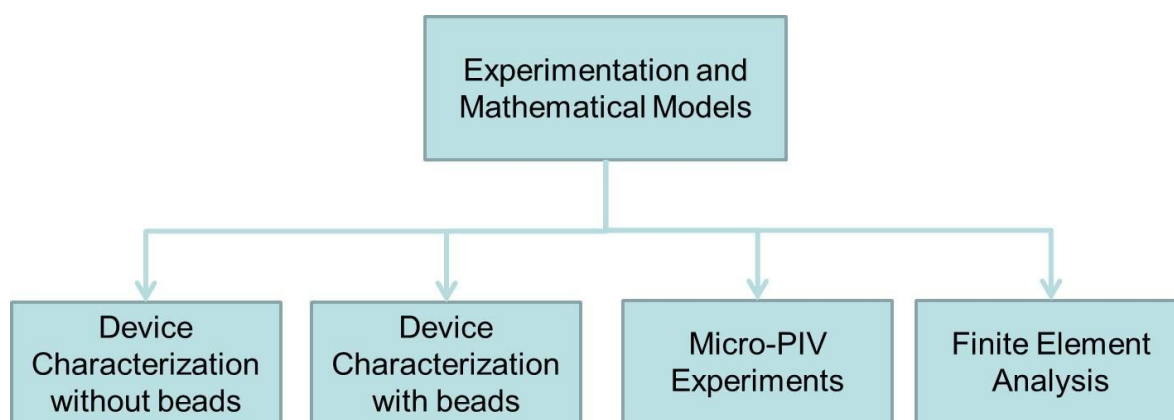


Figure 4.1: Flowchart of the experimental approaches carried out in this project.

4.1.1 Device Characterization without Beads

During experimentation, the fluid medium had to be controlled with precision to determine the optimal operating parameters of the micro-fluidic devices. In order to achieve the desired control, two syringe pumps (New Era Pump System NE-1000, see figure 4.2) were employed. The pumping accuracy of the two syringe pumps was near 98% of the specified pump/withdraw rate.



Figure 4.2: New Era Syringe Pump model NE-1000 (photo courtesy of New Era Pump Systems, Inc.).

The syringe pumps were employed to control the Phosphate-buffered saline (HyClone Dulbecco's Phosphate Buffered Saline) flow rate during the characterization of the device without beads. One of the syringe pumps infused a 50 $\mu\text{l/hr}$ flow rate through port 1 (figure 3.4) and the second syringe pump was used to control the flow rate at the exit of that channel in port 2. Port 2 was controlled to produce 4 different outflow rates which are 25%, 50%, 62.5% and 75% of the inflow rate. A case in which port 2 remained at atmospheric pressure was also studied. The two apertures of the lower channel, port 3 and port 4, were kept at atmospheric pressure. The PBS that exited the device through the different ports was collected and weighed to determine the flow rate through each port. These results helped us understand the flow distribution inside the channels and the results were used to validate computational models.



Figure 4.3: Pictures of the experimental set-up.

4.1.2 Device Characterization with Beads

Polystyrene beads with a diameter of $20 \pm 0.500 \mu\text{m}$ (Polysciences, Inc.) were used for these experiments. PBS was used as the suspension medium and it was preferred over distilled water because it diminishes the polystyrene beads susceptibility to adhere to the walls of the channel during experiments with PDMS micro-fluidic devices [40]. The particle concentration of the solution used for the experiments was 5.68×10^5 beads/mL. In these experiments, the suspended polystyrene beads were introduced using the syringe pump at port 1. The inlet and outlet conditions in these experiments were the same as in the device characterization experiments without beads. The suspended particles were introduced into the channel until all of the traps were filled. In the case when traps remained empty the experiments were stopped after 30 minutes of unsuccessful particle entrapment. A Nikon 80i reflected light microscope was used to qualitatively determine the functionality of the trapping sites of the micro-fluidic devices. The results allowed us to determine if the

geometry of the traps was adequate to trap and retain the beads and the percentage of functional traps for each inlet and outlet condition.

4.2 Micro-Particle Image Velocimetry (PIV)

Micro-PIV experiments required fluorescent markers (seed particles) suspended in a liquid flow to visualize the behavior of the flow. The marker chosen for these experiments was Nile red fluorescent polystyrene beads with 1 μ m in diameter (Invitrogen Inc.). The dye of the particle was chosen based on the current optical limitations of the experimental setup. The size of the particle was chosen based on the Stokes number criterion, the Brownian motion error and the depth of correlation (see sections 2.1.4-2.1.6 for more information). The particles were excited with a frequency doubled Nd:YAG laser (neodymium-doped yttrium aluminum garnet) at a wavelength of 532nm. The suspended solution has a concentration of approximately 1mL of particles (2% solids) for 10mL of PBS which yields a particle concentration of 3.31×10^9 beads/mL. This concentration yields approximately 5 particles per interrogation volume for the micro-PIV studies.

The micro-devices were prepared in the same manner as in the other experiments. The micro-fluidic device was placed on the inverted microscope and the syringe pump was used to induce the inlet flow rate of 50 μ L/hr. The suspended particles were introduced through port 1. The computer controlled laser was triggered to excite the particles and at the same time a high speed camera grabs double frame images of the particles flowing through the channel. The time between the frames was varied to obtain better results for the correlation. The times used varied from 125 μ s to 2000 μ s. 150 double frame images were

captured in each experimental run. The set of double frame images used varied depending on the velocity of the particles flowing through the channel. These images were processed with the tool software, Dantec Studio (Dantec Dynamics, Skovlunde, Denmark). Figure 4.4 shows the process flow of the experiment analysis. First, the data was analyzed using adaptive correlation which yielded velocity vectors for each seed particle from the double frame images. Then a vector masking tool was used to only consider the area of the channel for the subsequent analysis. A statistical analysis was performed to find the average velocity vector per interrogation area. Each interrogation area is composed of 32x32 pixels. The actual dimension of each interrogation area depends on the magnification of the objective in the microscope. Figure 4.5 demonstrates the double frame images obtained from the micro-PIV and the velocity field from the correlation of those images. The data was then examined using a MatLab script to determine the velocity profiles in different parts of the micro-fluidic device. The results obtained from these experiments were used to validate a mathematical model from COMSOL. Figure 4.6 shows the three of the most important parts of a micro-PIV system.

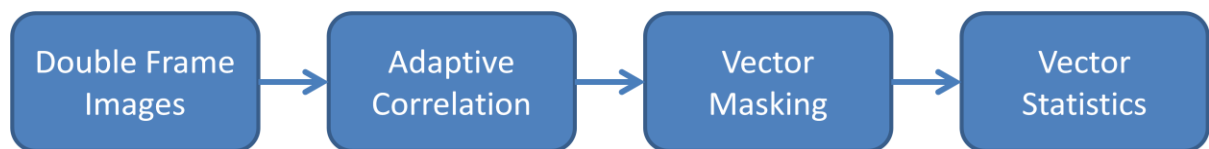


Figure 4.4: Process flow of the analysis of the experimental data from the micro-PIV.

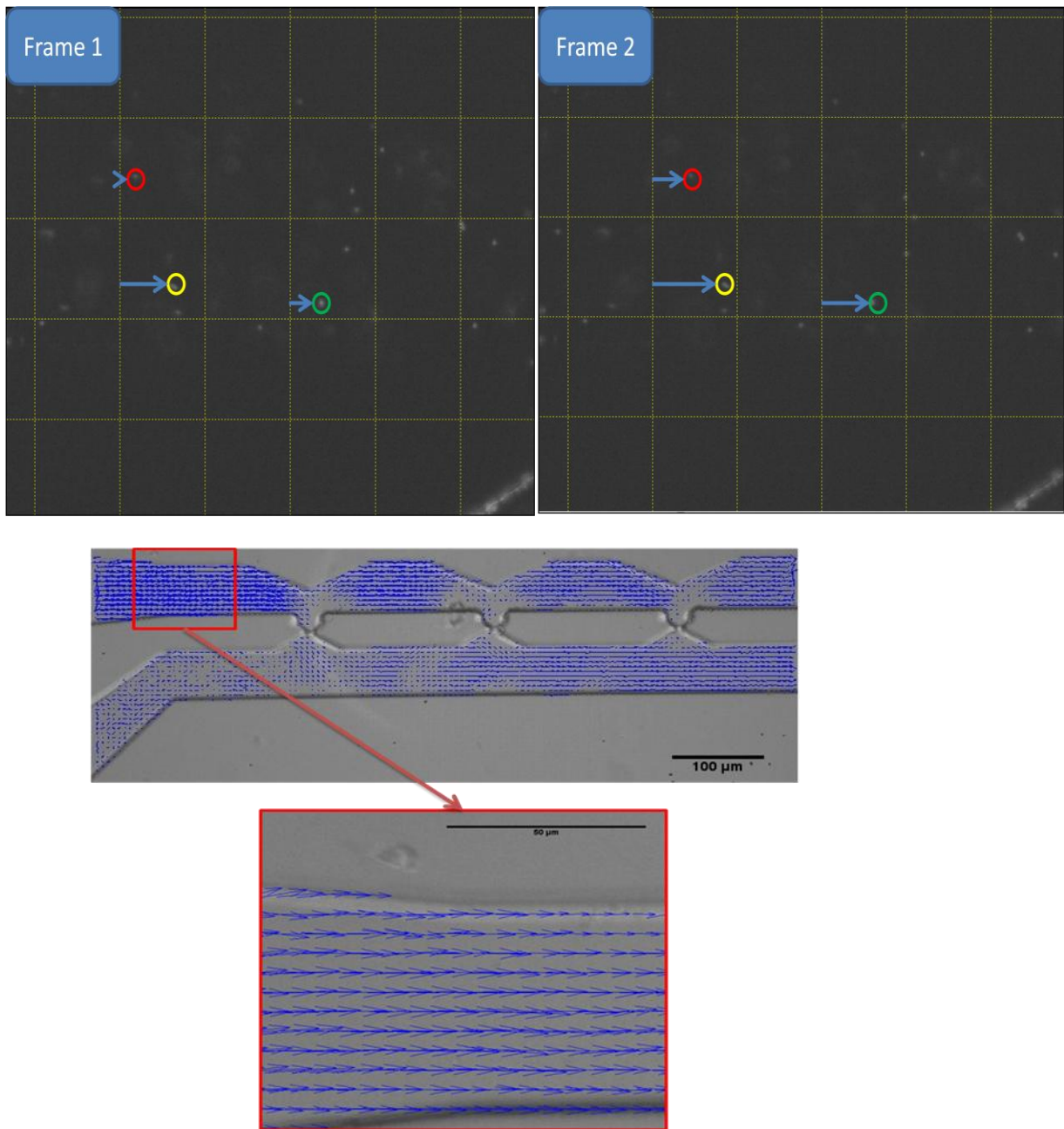


Figure 4.5: Double frame images and vector velocity field results from a micro-PIV experimental run.

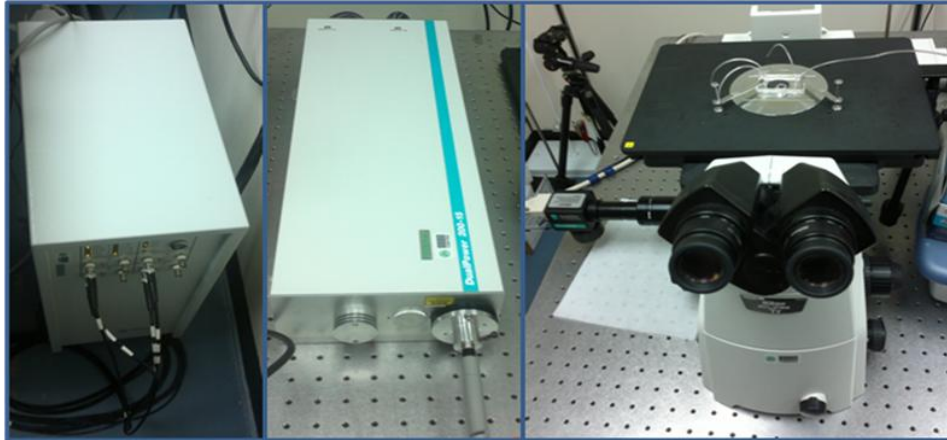


Figure 4.6: (Left) PIV control unit (Dantec Dynamics). (Center) The 532nm Nd:YAG laser (Dantec Dynamics). (Right) An inverted microscope (Nikon Eclipse Ti-U) with a lateral camera (Dantec Dynamics).

4.3 Finite Element Analysis

COMSOL Multiphysics (COMSOL, Inc., Burlington, MA) was the computational software used for the finite element analysis of the micro-fluidic channel under the various operating conditions. The software has predefined modules for various types of analysis. This software is very versatile and powerful, but at the same time easy to use. This section describes the complete procedure used for the finite element analysis.

The first step was to specify the module used for the analysis. Figure 4.7 shows the GUI to specify the module, the model to be solved and the space dimension. The micro-electro-mechanical systems modules (MEMS modules) contains a submodule for micro-fluidic analysis. The Stokes flow model was chosen because it serves as an approximation for the system analyzed. The Stokes module simplifies the Navier-Stokes equation and it uses less computational resources to run the mathematical analysis. The second step was to specify the dimension type of the analysis (e.g. 1D, 2D, 3D). For our purposes, a 2D

geometry was imported from AutoCad 2011 (Autodesk, San Rafael, CA) and a 3D geometry was created for the analysis by simply extruding the 2D geometry with a distance of 30 μm .

Figure 4.8 shows the 3D geometry in COMSOL.

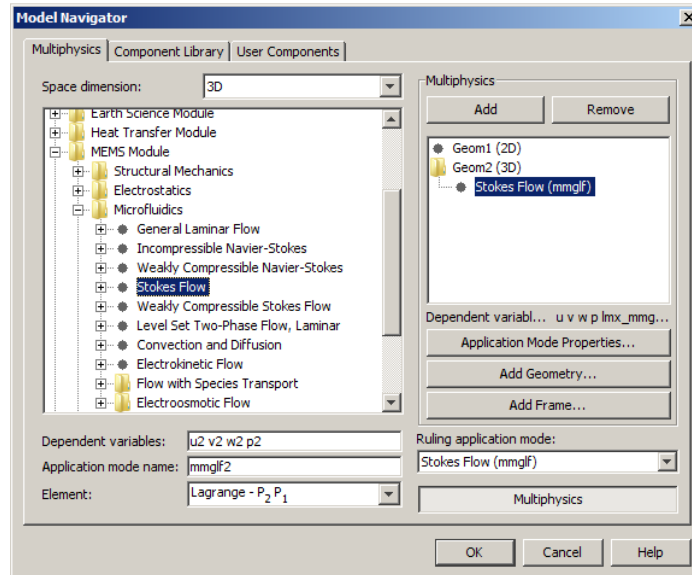


Figure 4.7: Initial COMSOL GUI to specify the module, the model and the geometry to be analyzed.

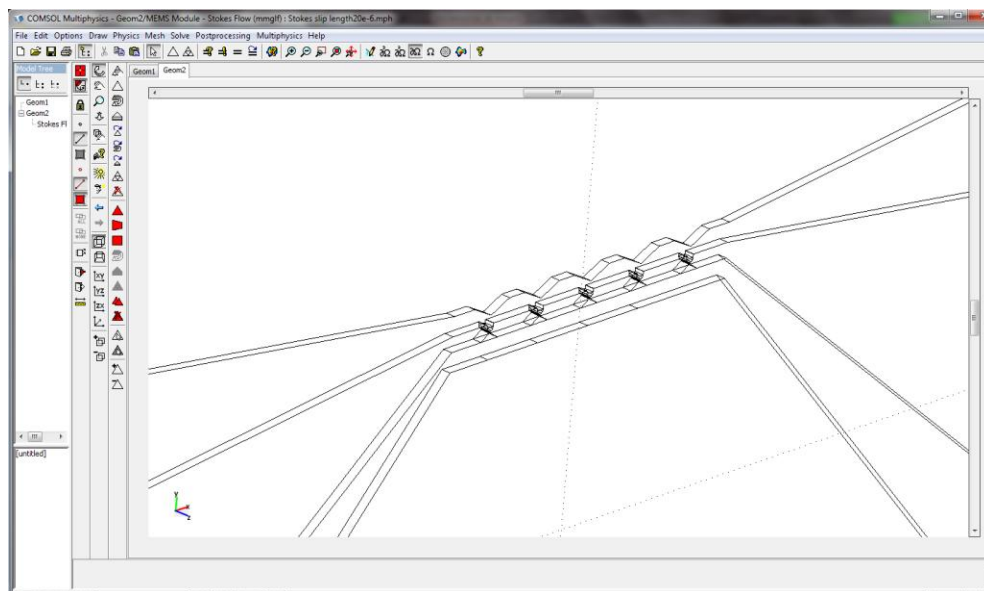


Figure 4.8: 3D geometry of the micro-fluidic channel in COMSOL.

Once the 3D geometry was defined, the subdomain properties were specified. The only material in the entire domain of the geometry (the insides of the micro-channel) is PBS. The properties of PBS are very similar to that of water, hence, the density and the dynamic viscosity used for the analysis were that of water at room temperature ($\rho = 998.08 \text{ kg/m}^3$, $\mu = 9.78 \times 10^{-4} \text{ Pa}\cdot\text{s}$). The next step was to specify the boundary conditions. Three types of boundary conditions were used inlet, outlet and wall. In the inlet boundary condition, the laminar inflow option was selected. The volumetric flow rate varied depending on the case under study. The values of the volumetric flow rates as a function of case study are depicted in table 4.1. There were also 8 outlet boundary conditions specified for port 2 and the values can be seen in table 4.1. The remaining outlet ports were set at atmospheric pressure. The boundary condition at the PDMS walls was varied from no slip to slip lengths up to $15 \mu\text{m}$. The boundary condition at the glass wall was also varied from no slip to slip lengths of a few microns. These models were then compared to the experimental values obtained from the micro-PIV to find the best fit.

Table 4.1: Port 1 and port 2 boundary conditions for each mathematical model.

Case / Boundary Conditions	Inlet (Port 1)	Outlet (Port 2)
Case 1 (unrestricted)	$1.3889 \times 10^{-11} \text{ m}^3/\text{s}$ (50 $\mu\text{L/hr}$)	0 Pa
Case 2 (25% restriction)	$1.3889 \times 10^{-11} \text{ m}^3/\text{s}$ (50 $\mu\text{L/hr}$)	$3.47225 \times 10^{-12} \text{ m}^3/\text{s}$ (12.5 $\mu\text{L/hr}$)
Case 3 (50% restriction)	$1.3889 \times 10^{-11} \text{ m}^3/\text{s}$ (50 $\mu\text{L/hr}$)	$6.9445 \times 10^{-12} \text{ m}^3/\text{s}$ (25 $\mu\text{L/hr}$)
Case 4 (75% restriction)	$1.3889 \times 10^{-11} \text{ m}^3/\text{s}$ (50 $\mu\text{L/hr}$)	$1.04168 \times 10^{-11} \text{ m}^3/\text{s}$ (37.5 $\mu\text{L/hr}$)
Case 5 (62.5% restriction)	$1.3889 \times 10^{-11} \text{ m}^3/\text{s}$ (50 $\mu\text{L/hr}$)	$8.68063 \times 10^{-12} \text{ m}^3/\text{s}$ (31.25 $\mu\text{L/hr}$)
Case 6 (29.6875% restriction)	$1.3889 \times 10^{-11} \text{ m}^3/\text{s}$ (50 $\mu\text{L/hr}$)	$4.1233 \times 10^{-12} \text{ m}^3/\text{s}$ (14.84375 $\mu\text{L/hr}$)
Case 7 (29.6875% restriction)	$2.7778 \times 10^{-11} \text{ m}^3/\text{s}$ (100 $\mu\text{L/hr}$)	$8.24659 \times 10^{-12} \text{ m}^3/\text{s}$ (29.6875 $\mu\text{L/hr}$)
Case 8 (29.6875% restriction)	$6.9445 \times 10^{-12} \text{ m}^3/\text{s}$ (25 $\mu\text{L/hr}$)	$2.06165 \times 10^{-12} \text{ m}^3/\text{s}$ (7.421875 $\mu\text{L/hr}$)

Subsequently, the domain was meshed using the free mesh parameter which creates a volumetric mesh of tetrahedrons. The mesh was composed of almost 85,000 volumetric elements in the entire domain. Figure 4.9 shows an example of a meshed domain of the micro-fluidic channel.

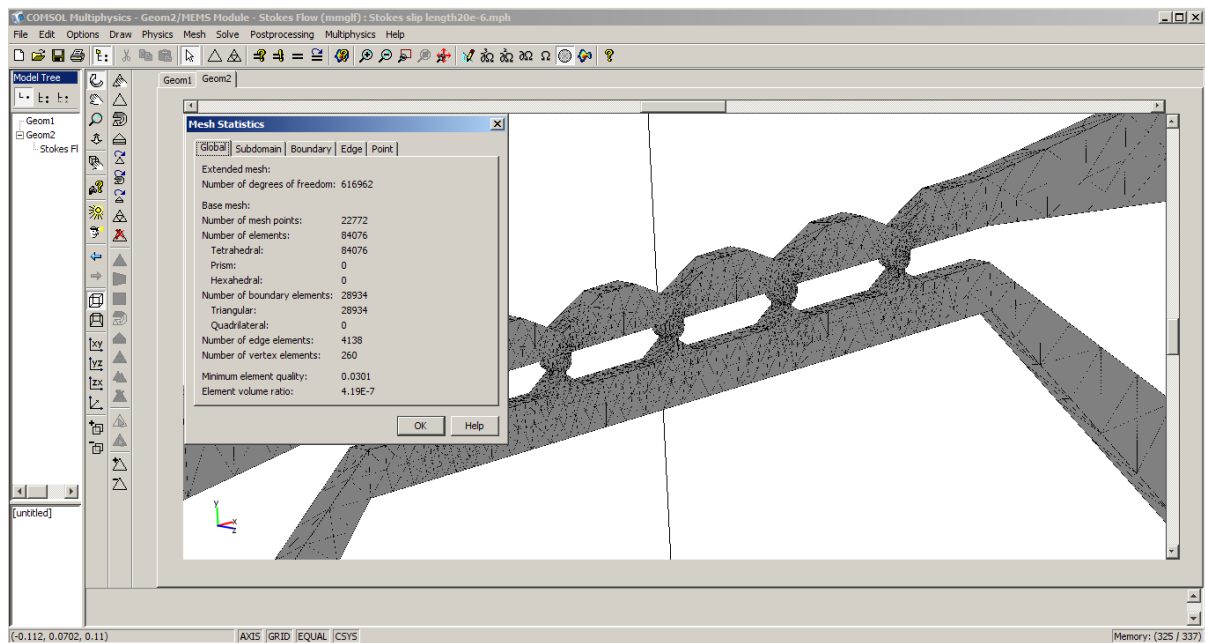


Figure 4.9: Volumetric mesh of the 3D geometry of the micro-fluidic channel.

Finally, the computational model was solved using the built-in solver. The results were plotted as slice plots of pressure and velocity field in the domain. Graphs of velocity profiles were plotted to compare with micro-PIV results. Flow rates at the traps and ports were determined using boundary integrations. Figure 4.10 shows the velocity field slice for the mathematical model of the studied micro-channel at a height of $15\ \mu\text{m}$.

Different geometries were studied in which traps were obstructed with $20\ \mu\text{m}$ spheres (see figure 4.11) to inspect the effects in the flow when beads are captured at the trapping sites.

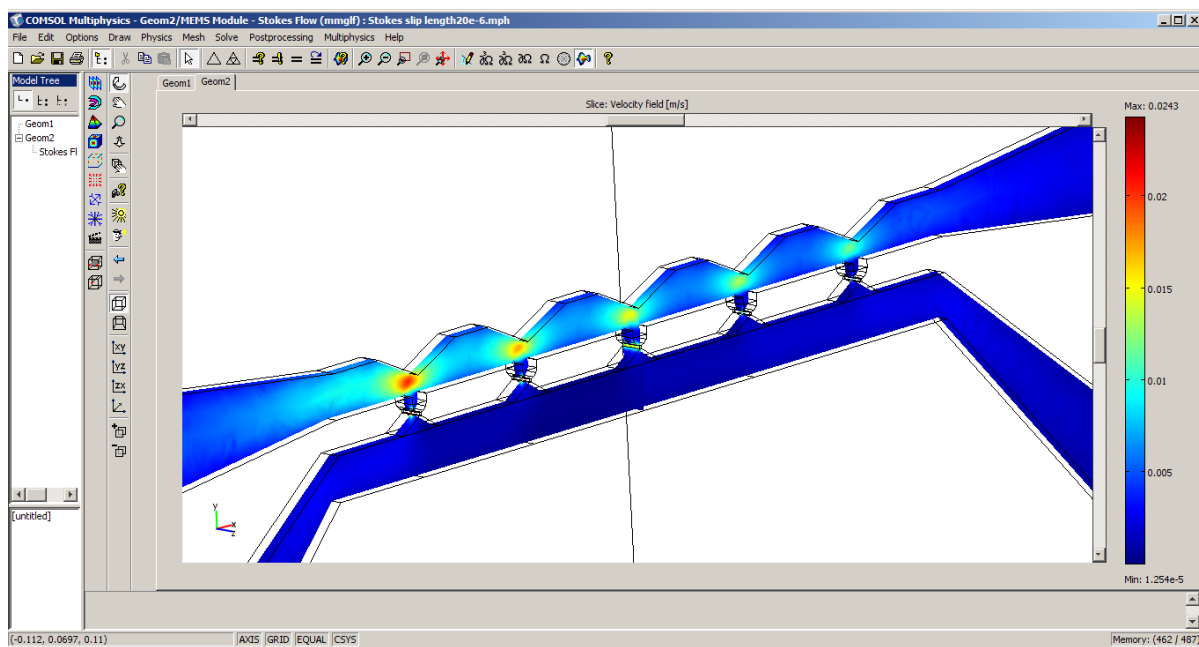


Figure 4.10: Velocity field slice plot of the studied micro-fluidic channel.

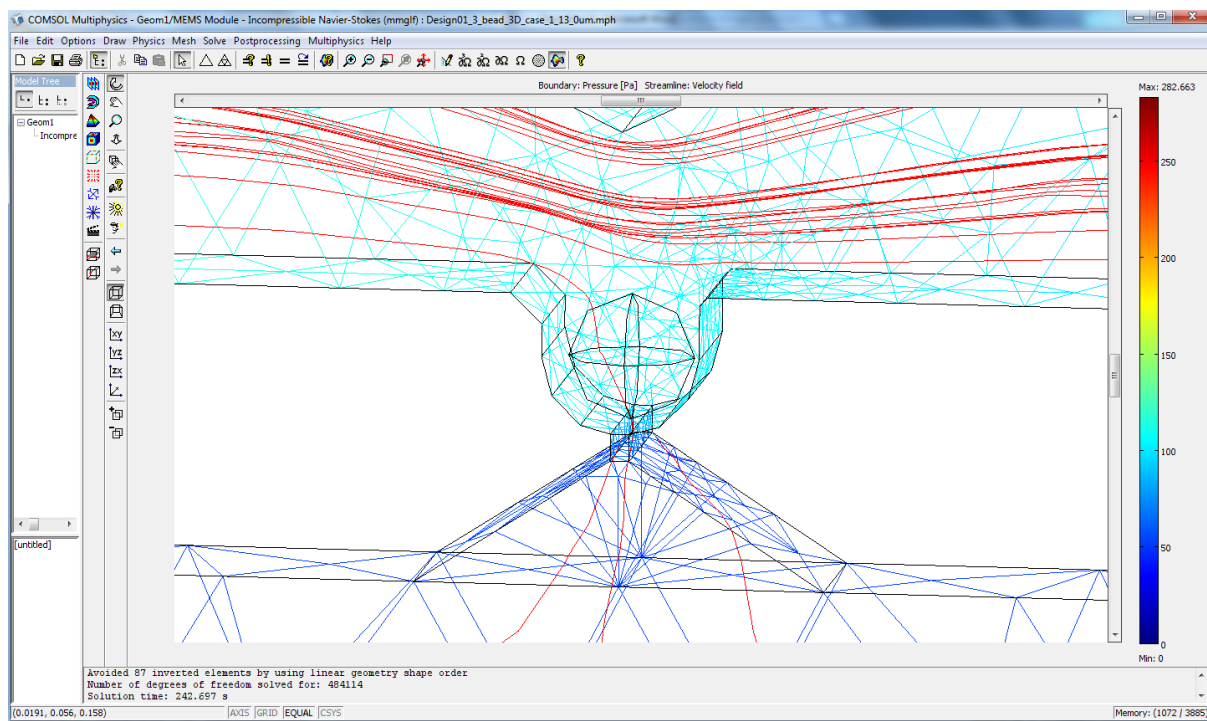


Figure 4.111: Pressure plot and streamlines of studied micro-fluidic channel with 20 μm sphere.

CHAPTER 5

This chapter presents and discusses the results of the experiments and finite element analysis discussed in chapter 4. The main purpose of the experiments was to validate a computational model and from that model obtain a design parameter that assures successful bead entrapment. This parameter will be helpful in the design of high-throughput devices in the near future.

5.1 COMSOL models comparison

Earlier in this document it was stated that for simulation purposes the Stokes flow model could be used instead of the Incompressible Navier-Stokes model to save computational resources and time. This section proves that the results obtained from both models are identical and that the time to solve the simulations using Stokes flow model was 10% of the time required using the Navier-Stokes model. All the simulations were solved using the same COMSOL version and the same hardware.

Figure 5.1 and 5.2 demonstrate that both models yield an identical pressure plot for the same boundary and physical conditions of case 1. The highest pressure in the incompressible Navier-Stokes model was 277.411 Pa and the highest pressure in the Stokes flow model was 277.302 Pa. Table 5.1 shows the results for the volumetric flow rate at the traps and the ports of the device for both models. There is no appreciable difference between the results of the volumetric flow rates of the models. A comparison of the velocity profile in the longitudinal direction is also included in figure 5.3. These velocity profiles were obtained from the red line demonstrated in figure 5.1 and 5.2. The graphs show that the velocity

profiles of both models are identical. It is clear that the Stokes flow model and the incompressible Navier-Stokes model have identical results. The difference between the models is the time consumed by each model to obtain a solution. The incompressible Navier-Stokes model required 390 seconds to solve the problem while the Stokes flow model only needed 44 seconds.

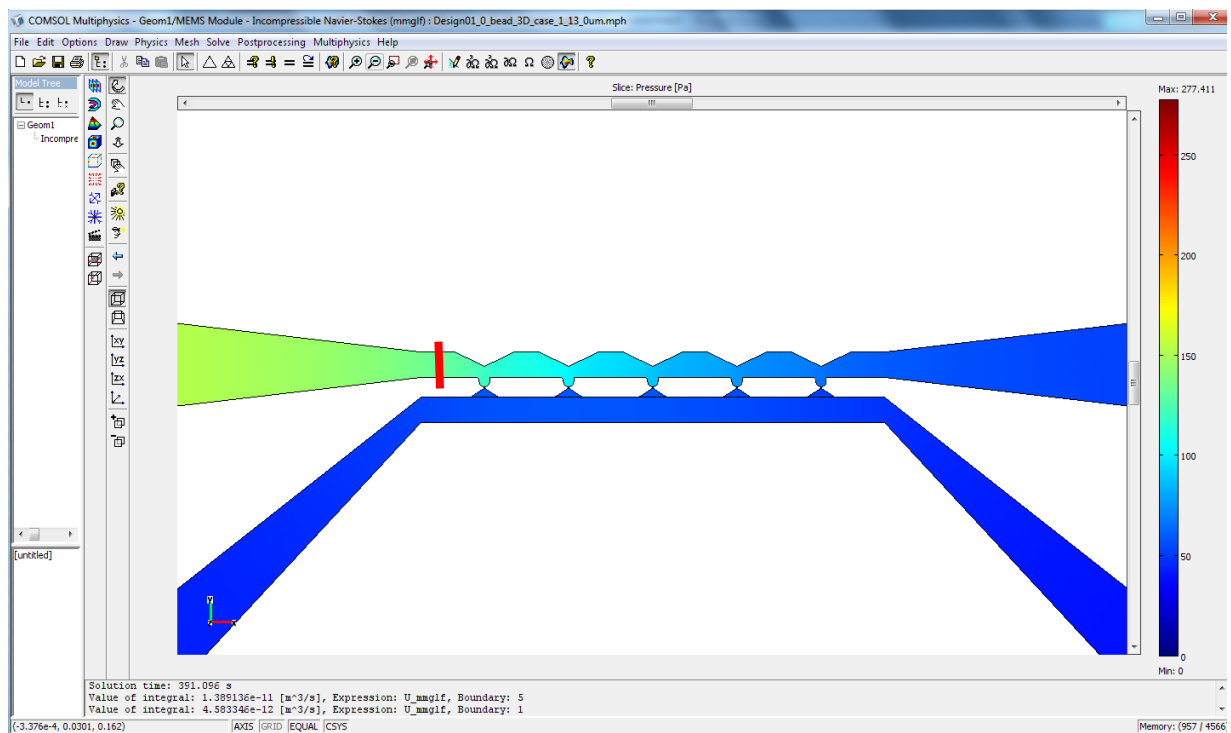


Figure 5.1: Case 1 (port 2 unrestricted) pressure plot using the incompressible Navier-Stokes model.

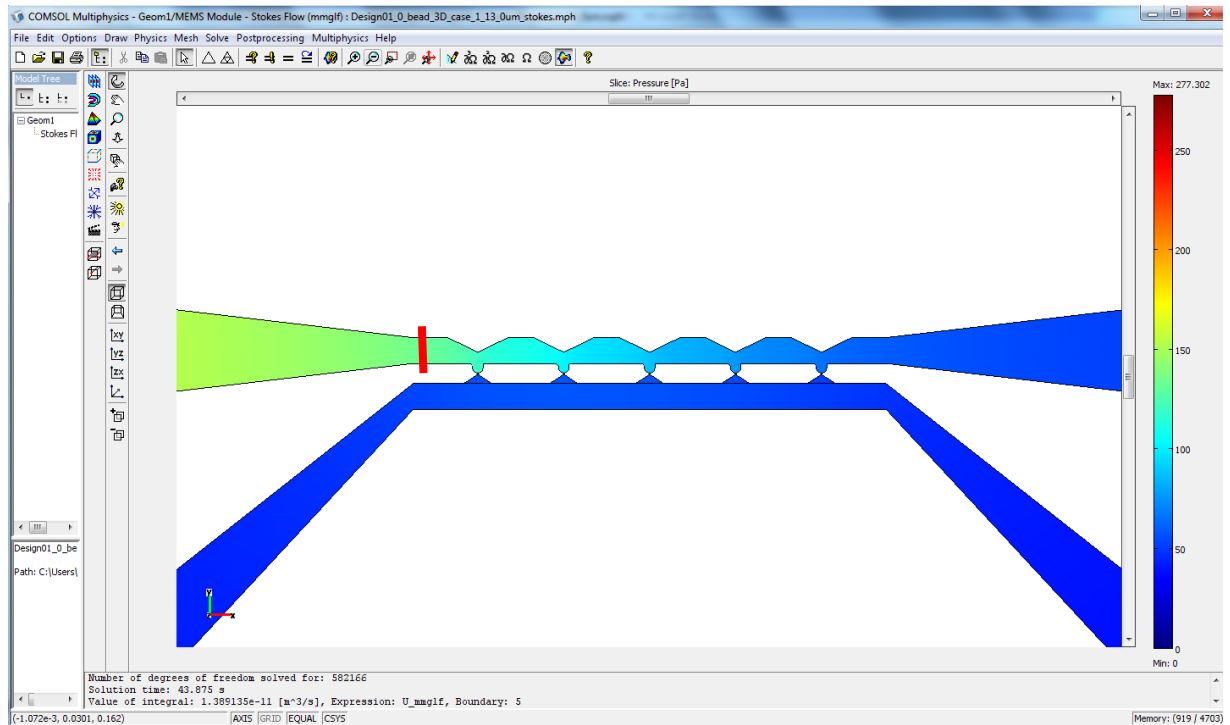


Figure 5.2: Case 1 (port 2 unrestricted) pressure plot using the Stokes flow model.

Table 5.1: Volumetric flow rate results of the incompressible Navier-Stokes model and the Stokes flow model.

Volumetric flow rate	Incompressible Navier-Stokes	Stokes flow
Q Port 1 [m ³ /s]	1.39E-11	1.39E-11
Q Port 2 [m ³ /s]	4.58E-12	4.58E-12
Q Port 3 [m ³ /s]	5.83E-12	5.82E-12
Q Port 4 [m ³ /s]	4.14E-12	4.14E-12
Q trap 1 [m ³ /s]	3.13E-12	3.13E-12
Q trap 2 [m ³ /s]	2.24E-12	2.23E-12
Q trap 3 [m ³ /s]	1.56E-12	1.55E-12
Q trap 4 [m ³ /s]	1.12E-12	1.12E-12
Q trap 5 [m ³ /s]	5.27E-13	5.26E-13

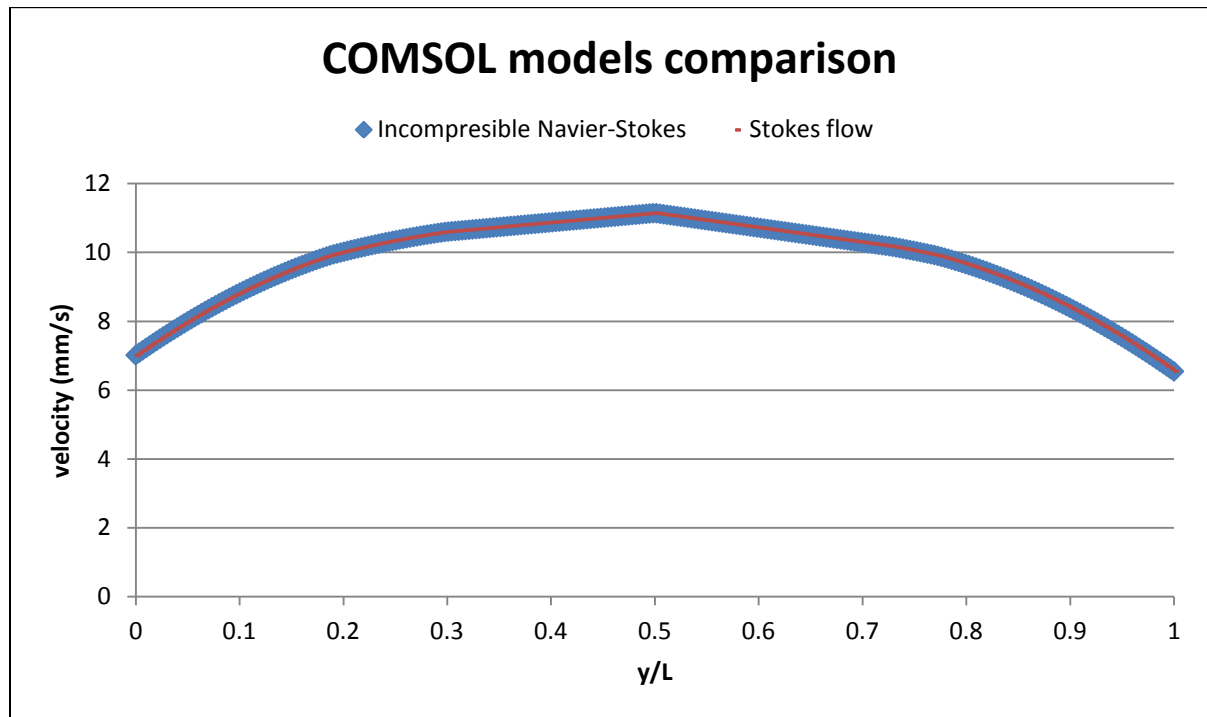


Figure 5.3: Velocity profiles in the longitudinal direction for the incompressible Navier-Stokes model and the Stokes flow model.

5.2 Micro-PIV experiments vs. COMSOL results

The micro-PIV experiments were essential to completely validate the mathematical model obtained from COMSOL. The experimental parameters are shown in table 5.2. These experiments suggest that the micro-channel has a slip condition at the PDMS wall. In chapter 2, the no slip and slip length theory was discussed and some publications have shown that fluid slip can occur at PDMS walls while a no slip is expected in at the glass wall. The experiments were performed in an area just before the first trap (see figure 5.4). Figure 5.5 shows the micro-PIV experimental results and the COMSOL results of the velocity profile in the longitudinal direction of the upper channel before the first trap for a model with slip of 13

μm at the PDMS wall and no slip at the glass wall, a model with 20 μm slip length at all the walls and another model with no slip at all the walls. It is clear that the velocity profile has a parabolic shape. It also demonstrates that the best fit for the micro-PIV data is the model that has a 13 μm slip length at the PDMS walls and no slip at the glass wall. The best fit was also determined using least squares method. The sum of the squares of the residuals was 268 for the no slip model, 80 for the 20 μm slip length model and 0.024 for the 13 μm slip length and no slip model. Remember that the best fit is determined by the smallest sum of the squares of the residuals. The results of this method showed that the best fit was the model with 13 μm slip length at the PDMS and no slip at the glass wall. This is congruent with a previous study that showed that slip velocity can occur at PDMS walls [41]. This study also demonstrated that the glass wall has no slip [41]. This velocity profile is at the middle point of the channel height but it is not the velocity profile with the highest velocity. This is the result of asymmetrical boundary conditions at the walls of the channel. Figure 5.6 through 5.8 show contour plots of the COMSOL models in the same plane of the velocity profile of figure 5.5.

Table 5.2: Volumetric flow rate results of the incompressible Navier-Stokes model and the Stokes flow model.

fluorescent marker	1 μm Nile red polystyrene beads
Fluidic medium	DPBS
Port 1 volumetric flow rate	50 $\mu\text{L/hr}$
Objective magnification	20x
depth of correlation	12.1 μm
Time between pulses	1000 μs
Number of double frame images	150

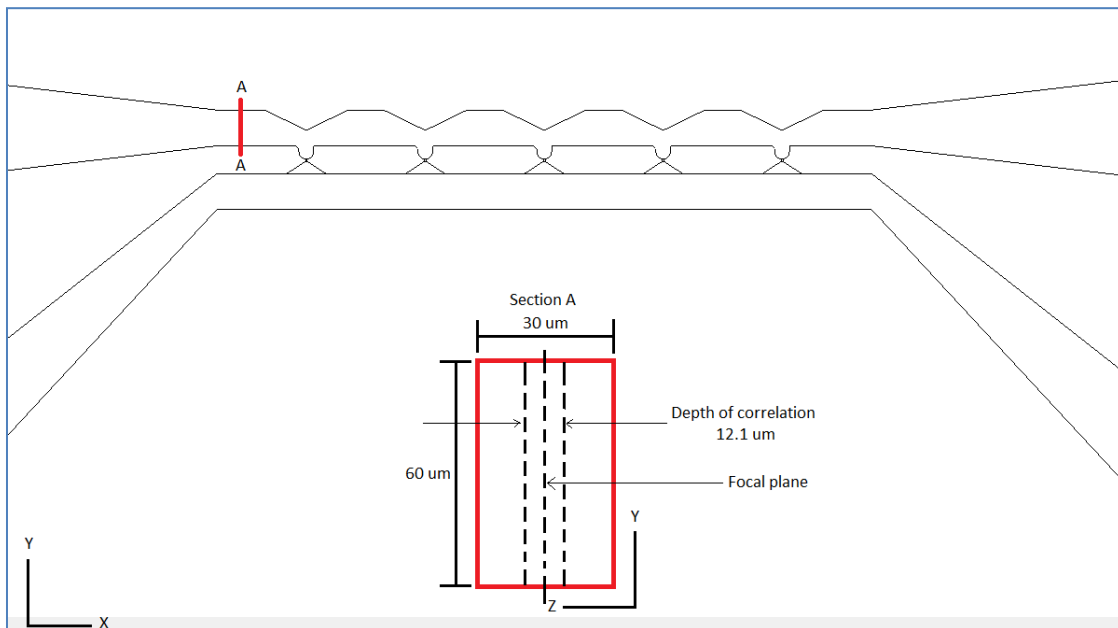


Figure 5.4: Region of interest for the micro-PIV experiments and the cross-sectional area of the region of interest with the depth of correlation.

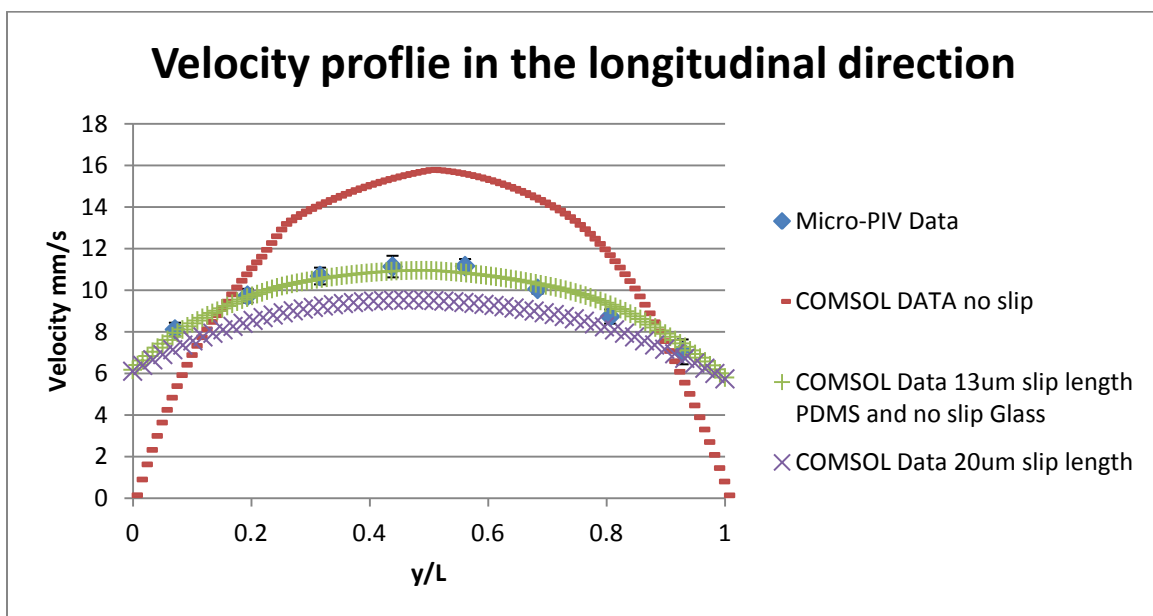


Figure 5.5: Graph of velocity profile in the longitudinal direction from the micro-PIV experiments (blue diamonds) compared to the corresponding velocity profile from the COMSOL model for case 1 (port 2 unrestricted) with 13 μm slip length at PDMS walls and no slip at glass wall (green plus sign), 20 μm slip length at all the walls (violet cross) and no slip at all the walls (red line).

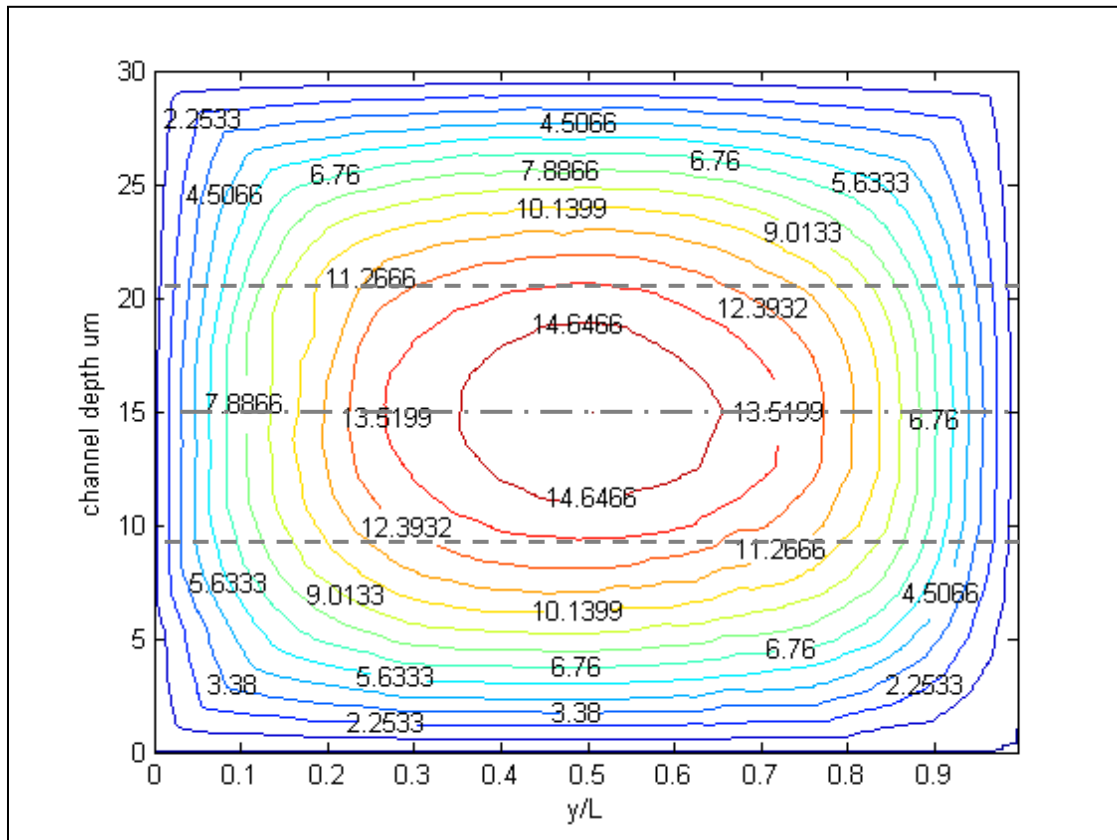


Figure 5.6: Contour plot of the region of interest for the COMSOL model with no slip at all the walls. The centerline represents the focal plane and the other two lines represent the depth of correlation.

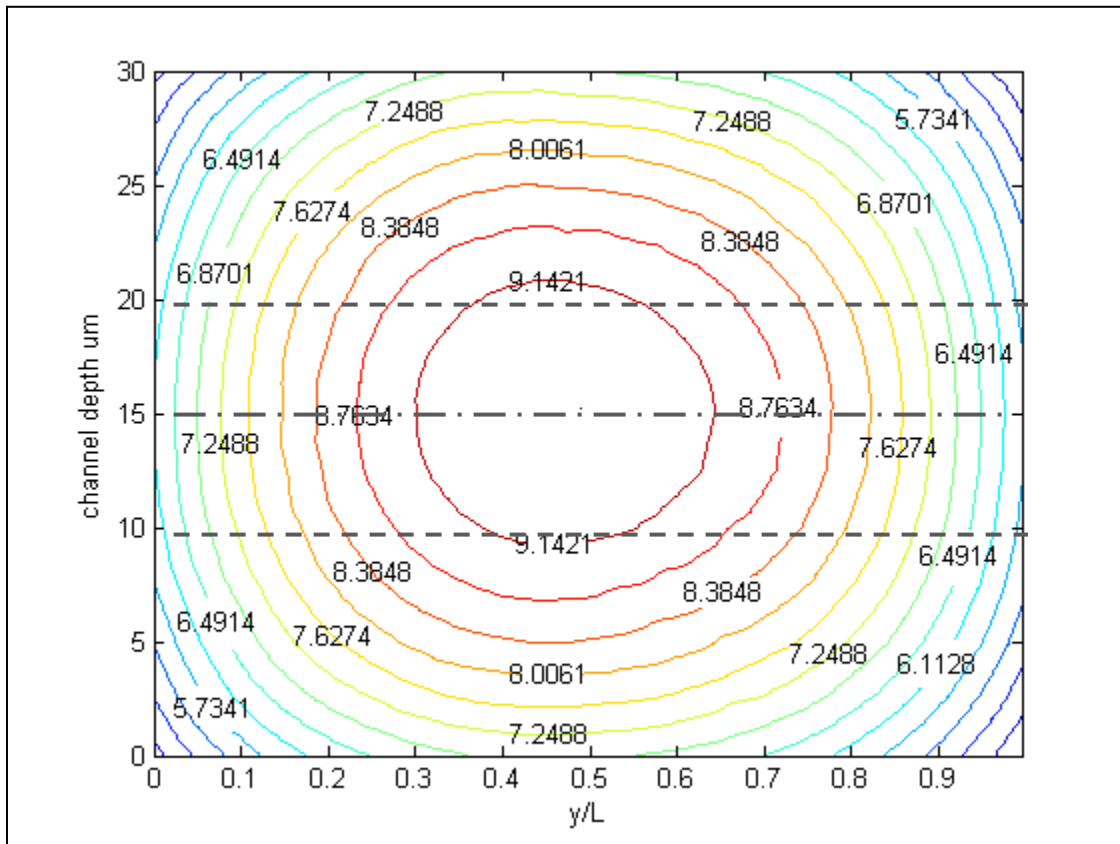


Figure 5.7: Contour plot of the region of interest for the COMSOL model with $20\ \mu\text{m}$ slip length at all the walls. The centerline represents the focal plane and the other two lines represent the depth of correlation.

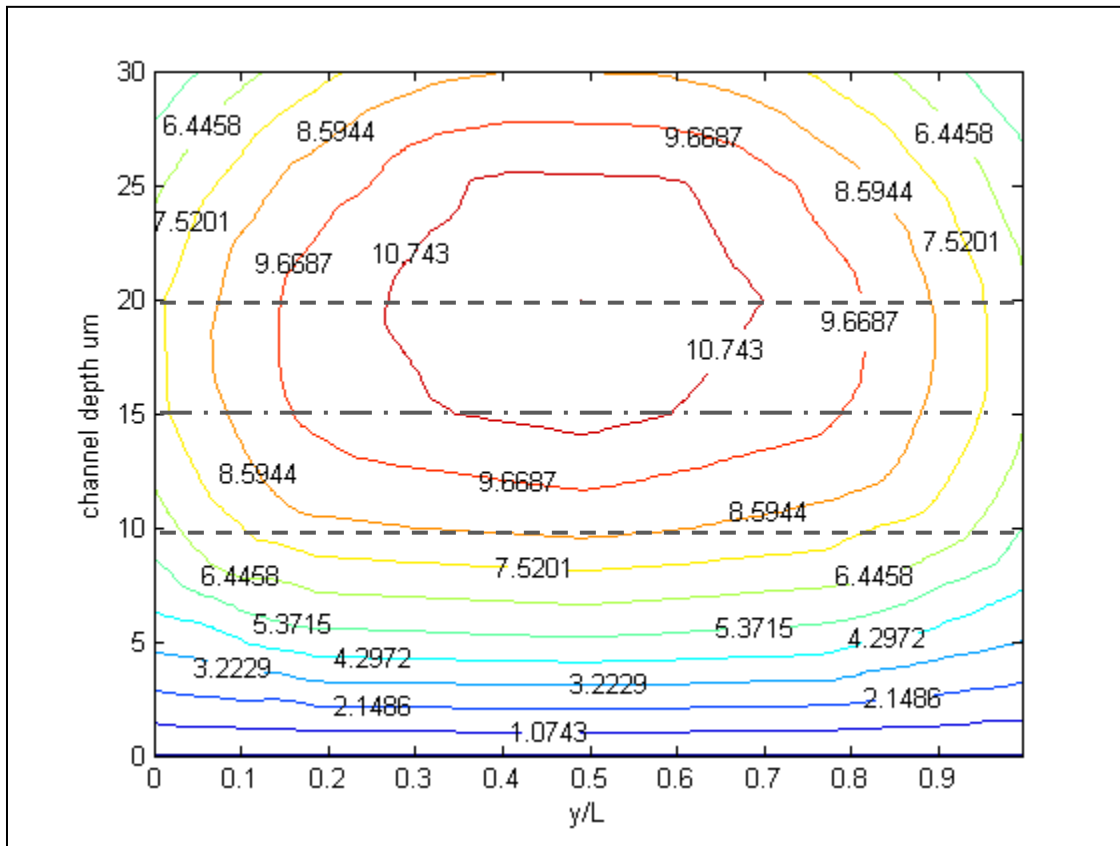


Figure 5.8: Contour plot of the region of interest for the COMSOL model with $13\ \mu\text{m}$ slip length at the PDMS wall and no slip at the glass wall. The centerline represents the focal plane and the other two lines represent the depth of correlation.

These contour plot demonstrates that the maximum velocity profile is at the center of the channel at the region of interest if the boundary conditions are symmetrical. If the boundary conditions are asymmetrical like in the case of $13\ \mu\text{m}$ slip length at the PDMS walls and no slip at the glass wall the maximum velocity profile shifts toward the PDMS wall. The depth of correlation was superimposed on the contour plots to show the extent of the depth of correlation. This shows that the micro-PIV measurements can deviate from the true

velocity profile and this deviation will produce errors in the measurements. This errors can be an important factor for the error bars shown in figure 5.5.

Figure 5.9 through 5.11 are surface plots of the same region of interest. These plots illustrate the symmetry of the velocity profile when the boundary conditions are symmetrical and also confirm the shift of the maximum velocity profile toward the top PDMS wall when the boundary conditions are asymmetrical. plane which clearly shows the asymmetric boundary conditions at the PDMS and glass walls. This velocity field distribution affects only the particles that are at different depths of the channel and not in different position with respect of the height of the channel.

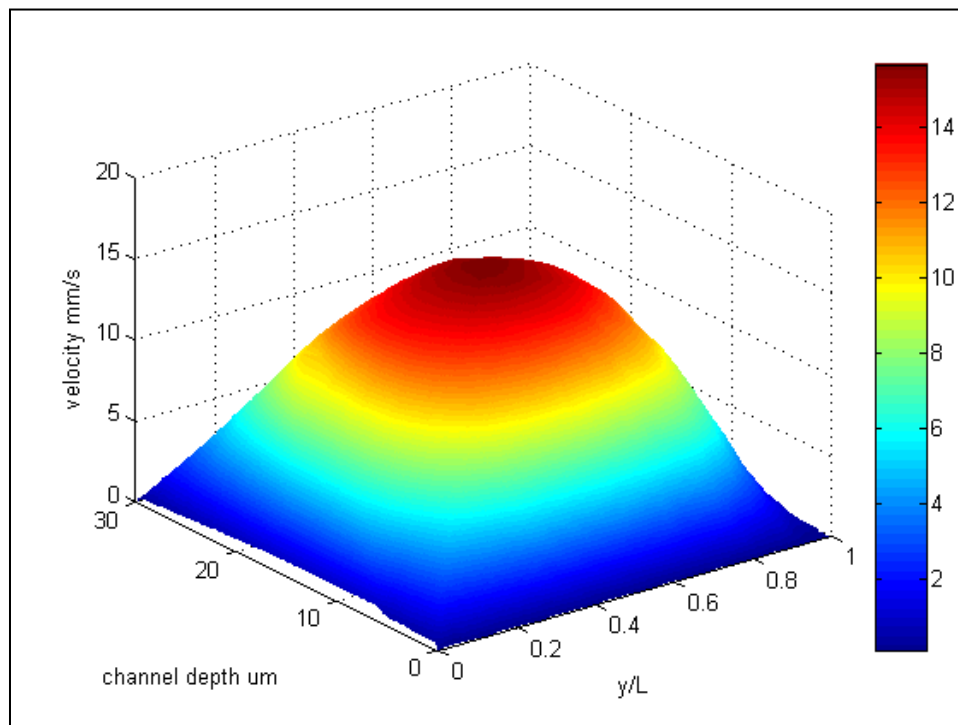


Figure 5.9: Surface plot of the region of interest for the COMSOL model with no slip at all the walls.

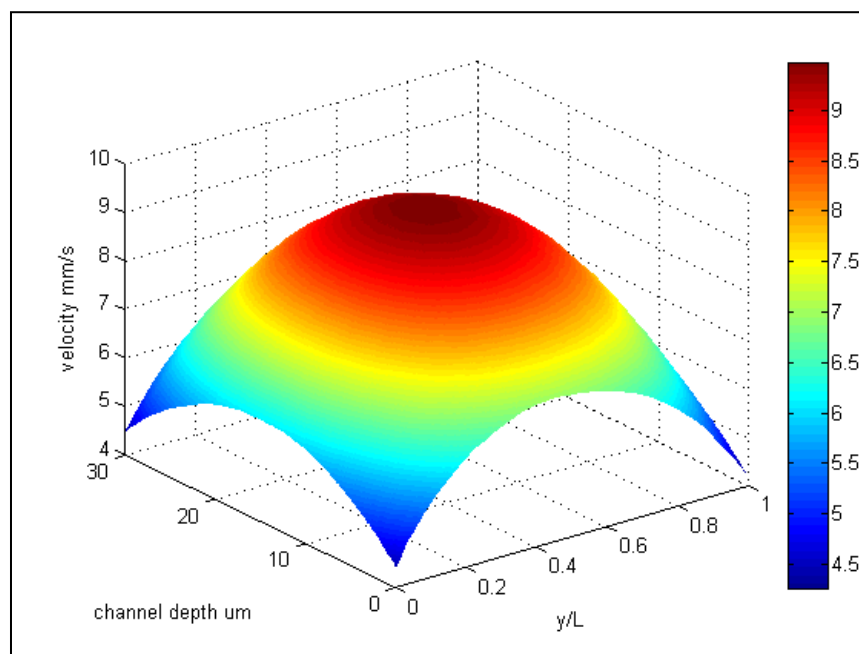


Figure 5.10: Surface plot of the region of interest for the COMSOL model with 20 μm slip length at all the walls.

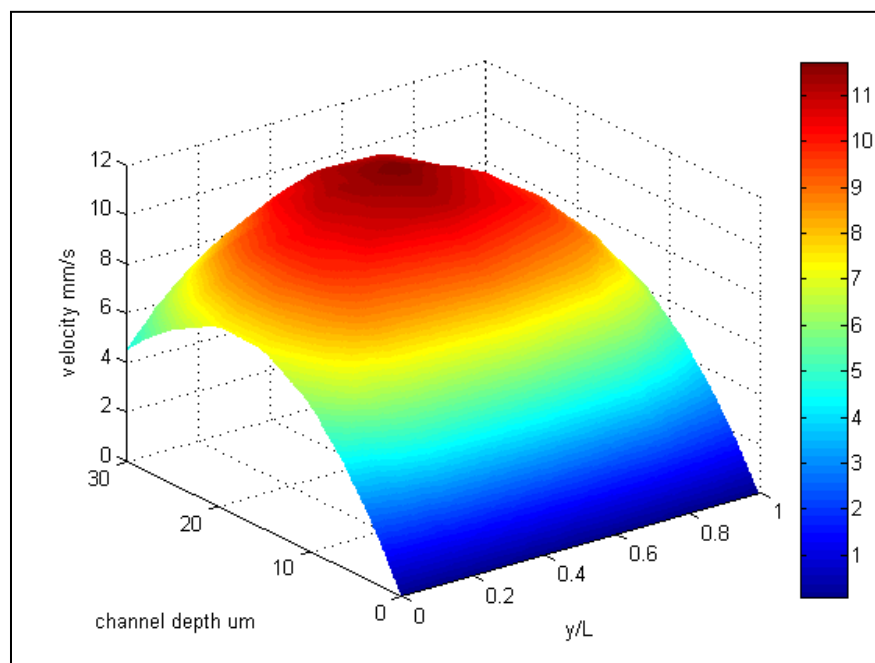


Figure 5.11: Surface plot of the region of interest for the COMSOL model with 13 μm slip length at the PDMS wall and no slip at the glass wall.

The results presented in this section confirmed the presence of slip length at the walls. The best fit for the micro-PIV data is a COMSOL model with asymmetrical boundary conditions at the walls. The PDMS walls have a 13 μm slip length and the glass wall has a no slip condition. The asymmetrical boundary conditions is responsible for the shift of the maximum velocity of the fluid in the region of interest toward the top PDMS wall.

5.3 Experiments without beads vs. COMSOL results

These experiments were essential in the validation of the mathematical model. The results of the COMSOL model demonstrated that the mass conservation and mass distribution had a similar value when compared to the experimental data. The comparison for cases 1, 2, 3 and 4 can be seen in figure 5.12 through figure 5.15. The standard deviation for some experiments was large but one factor that could have contributed to experimental errors was the environment particulate. This could have been an error because PBS was collected in small beakers and then weighed to determine the difference in mass from the beginning to the end of the experiments. During this process ambient particulate could have accumulated on the beakers. The mass extracted through each port was the size of a water drop, therefore, any dirt particle introduced into the collected PBS mass was going to affect the measurements. Another factor that contributed to a large standard deviation was that three different SU-8 molds were used to fabricate the channels and the heights and feature dimensions of the molds varied. The last possible factor for the standard deviation could be that particles partially obstructed the channel changing the flow distribution in the channel.

The graphs show that the simulations using the asymmetrical slip length model predicted similar outflows compared to the outflows obtained during experimentation. These results help confirm that the asymmetrical slip length model is the best model to describe the operation of the micro-fluidic device.

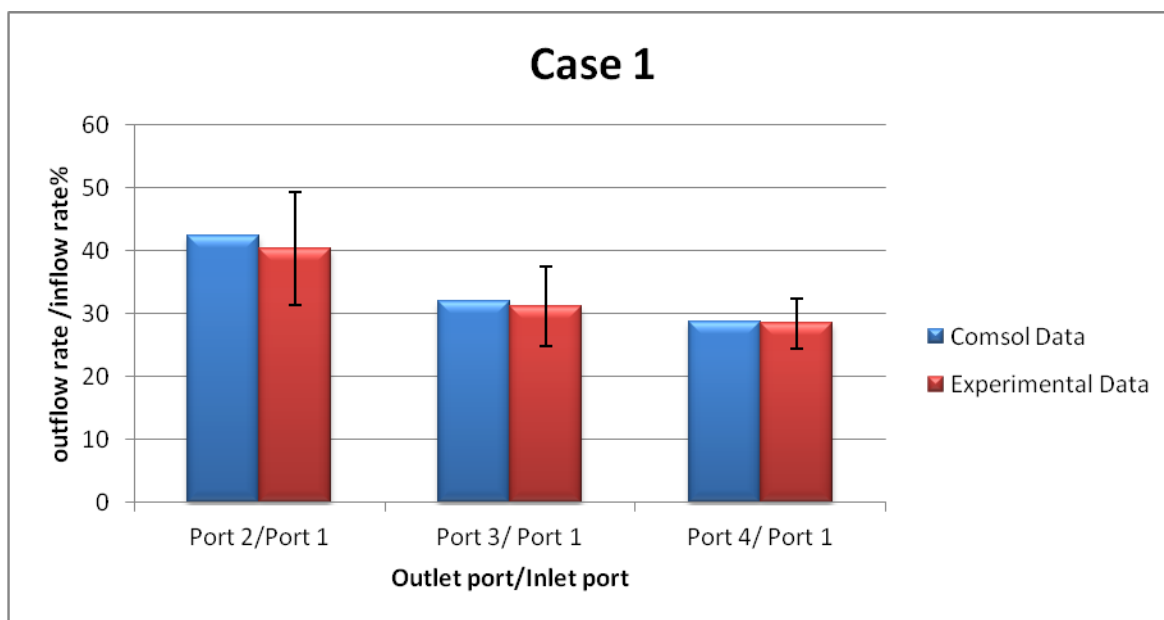


Figure 5.12: Graph of outflow rates from experiments of characterization without beads compare to outflow rates of COMSOL model for the case 1 (port 2 unrestricted).

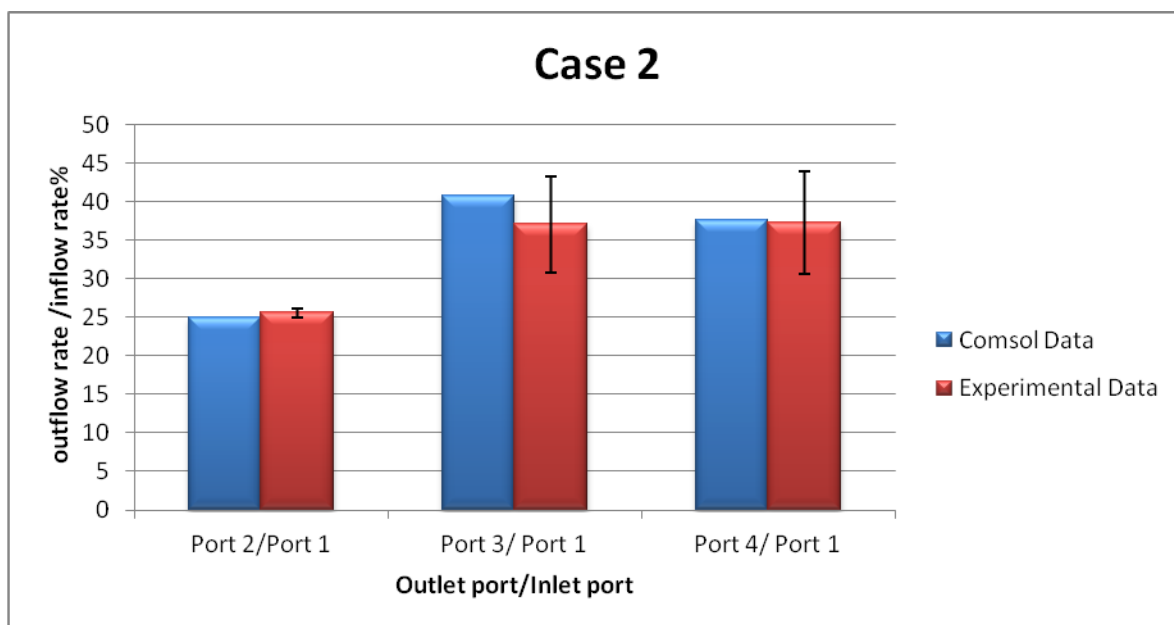


Figure 5.13: Graph of outflow rates from experiments of characterization without beads compare to outflow rates of COMSOL model for the case 2 (port 2 restricted to 25% of inflow rate).

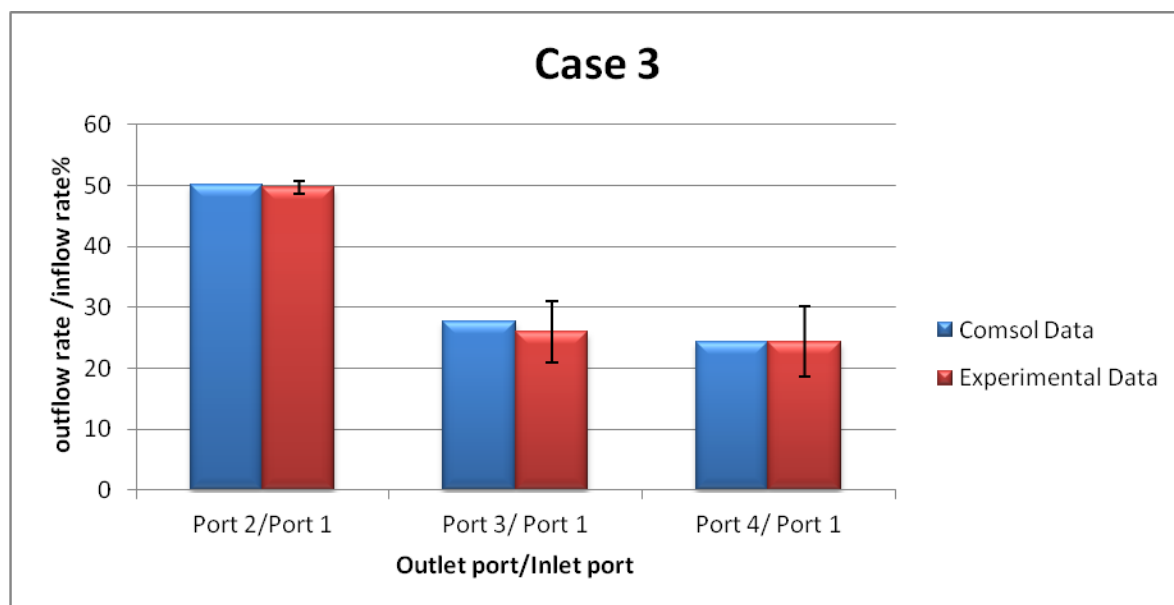


Figure 5.14: Graph of outflow rates from experiments of characterization without beads compare to outflow rates of COMSOL model for the case 3 (port 2 restricted to 50% of inflow rate).

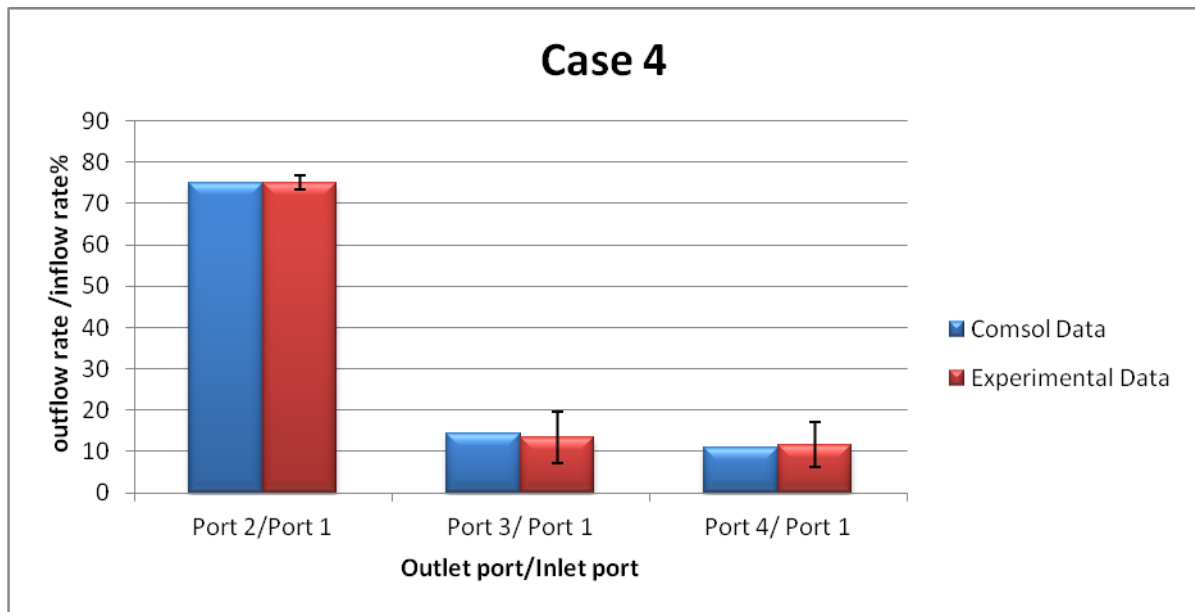


Figure 5.15: Graph of outflow rates from experiments of characterization without beads compare to outflow rates of COMSOL model for the case 4 (port 2 restricted to 75% of inflow rate).

5.4 Characterization experiments with polystyrene beads and COMSOL results

The characterization experiments with polystyrene beads were essential to determine if the geometry of the channel was capable of trapping and retaining the beads. Also, these experiments determined the operating parameters at which the beads were trapped. Based on these experiments and the data collected from the validated COMSOL model, we were able to see a tendency in one of the non-dimensional terms derived in Chapter 1, the velocity ratio ($V_{trap}/V_{channel}$). The data suggests that we can predict when the beads are going to get captured in the designated cavity, based on this non-dimensional parameter.

Figure 5.16 shows a micrograph of the micro-fluidic channel in which all the traps successfully trapped 20 μm beads. This micrograph is for the conditions of case 1 specified in table 4.1. The results of case 2 are demonstrated in figure 5.17. In this case it can be seen that multiple beads were trapped in the last trap site. This bead agglomeration could be caused by the restriction of the outflow in the upper channel. This restriction is 25% of the inflow rate.

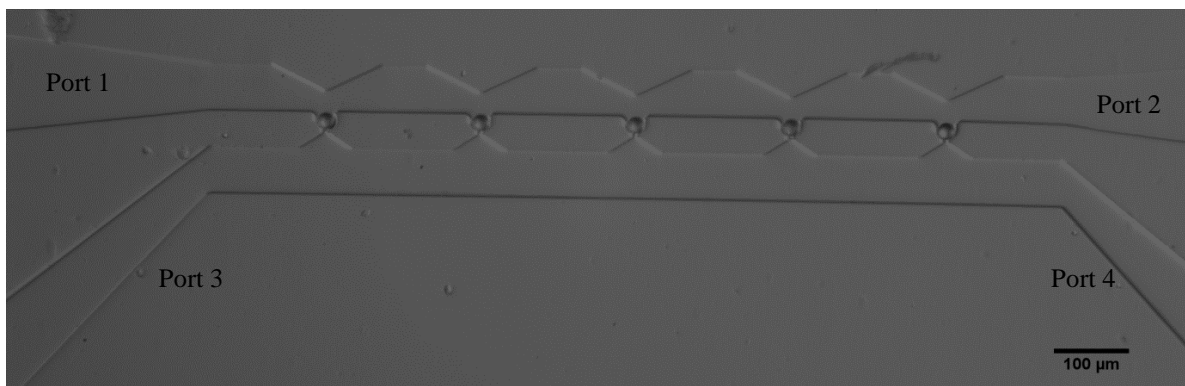


Figure 5.16: Micrograph of the experiment of the characterization with 20 μm beads for case 1.

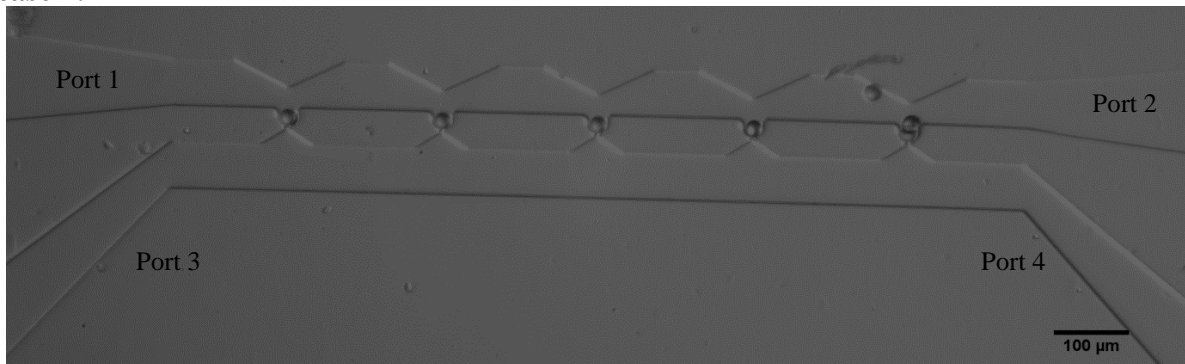


Figure 5.17: Micrograph of the experiment of the characterization with 20 μm beads for case 2.

Case 3 results are shown in figure 5.18. The result of this case is very similar to the results of case 1 and it is because the unrestricted flow rate at port 2 in case 1 is approximately 42% of the inlet flow rate and in case 3 the restricted flow rate is 50% of the

inflow rate. The results were expected to be comparable because the outflow rates are similar.

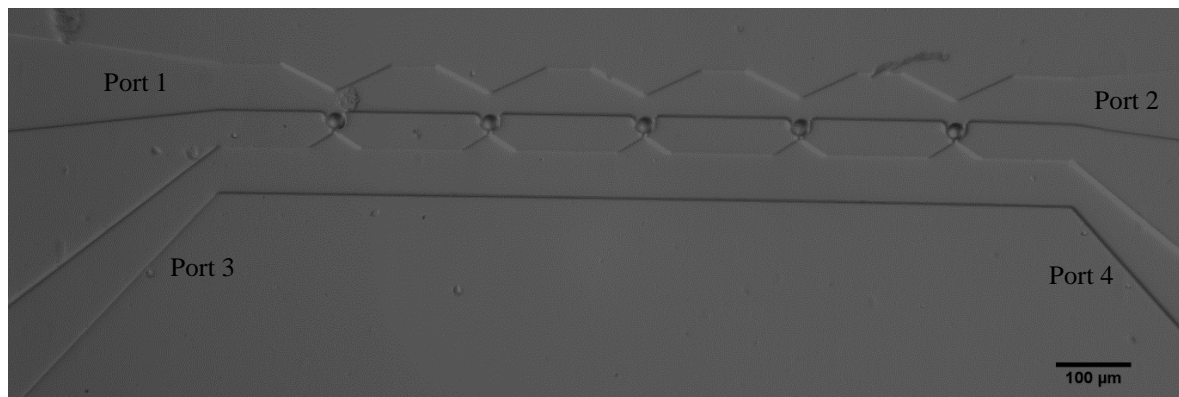


Figure 5.18: Micrograph of the experiment of the characterization with 20μm beads for case 3.

Figure 5.19 illustrates the results of case 4. In this case the port 2 restriction is 75% of the inlet flow rate. As it can be seen the last 2 traps are empty. Apparently, since 75% of the flow is leaving through port 2, there is not enough flow going through the last two traps, hence they remained empty during the experiments.

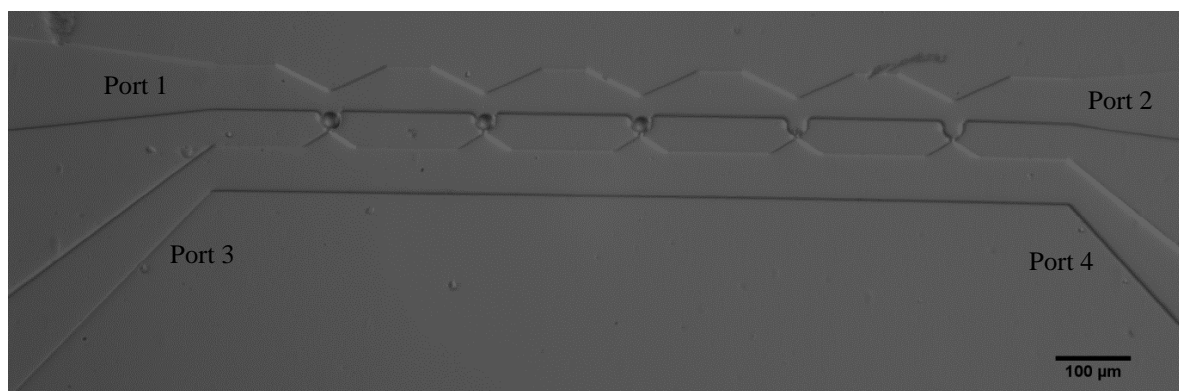


Figure 5.19: Micrograph of the experiment of the characterization with 20μm beads for case 4.

In case 5, the outflow rate at port 2 was selected to be in the middle of case 3 and case 4. The restriction in this case is 62.5% of the inflow rate and this condition yields a result in which only the last trap site remained empty. Figure 5.20 shows the micrograph of this case.

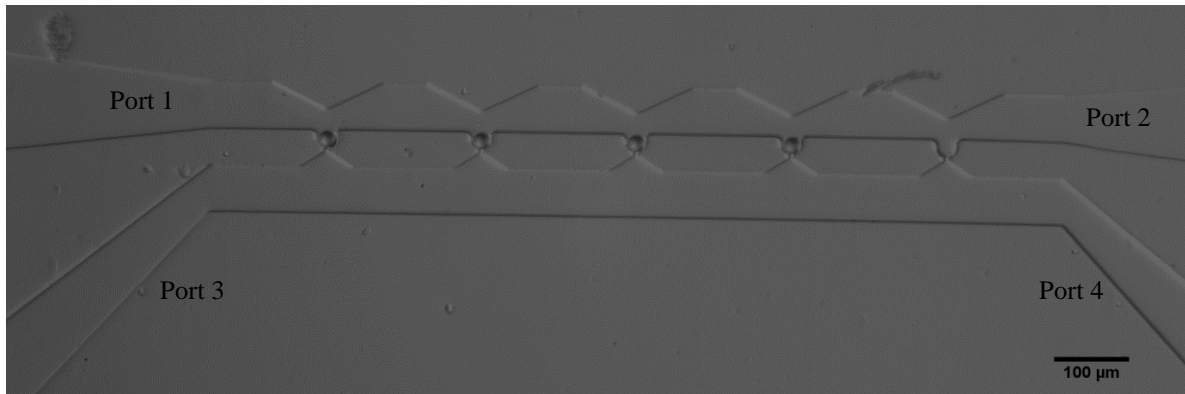


Figure 5.20: Micrograph of the experiment of the characterization with 20μm beads for case 5.

The following graph (figure 5.21) illustrates experimental data from the characterization with beads experiments. This data recollects the results of multiple experimental runs ($n=8$). The value of the bar plot is the median number of beads trapped in the experiments and the error bars represents the maximum and minimum number of beads trapped in experiments. The results of the case in which port 2 was restricted to 25% show that up to 11 beads were trapped during experimentation. The device has only 5 traps, the fact that 11 beads were trapped during experiments means that more than 1 bead was trapped at different trap site. Usually when this happens the beads start to agglomerate in the channel obstructing the movement of other beads until the experiment is finished.

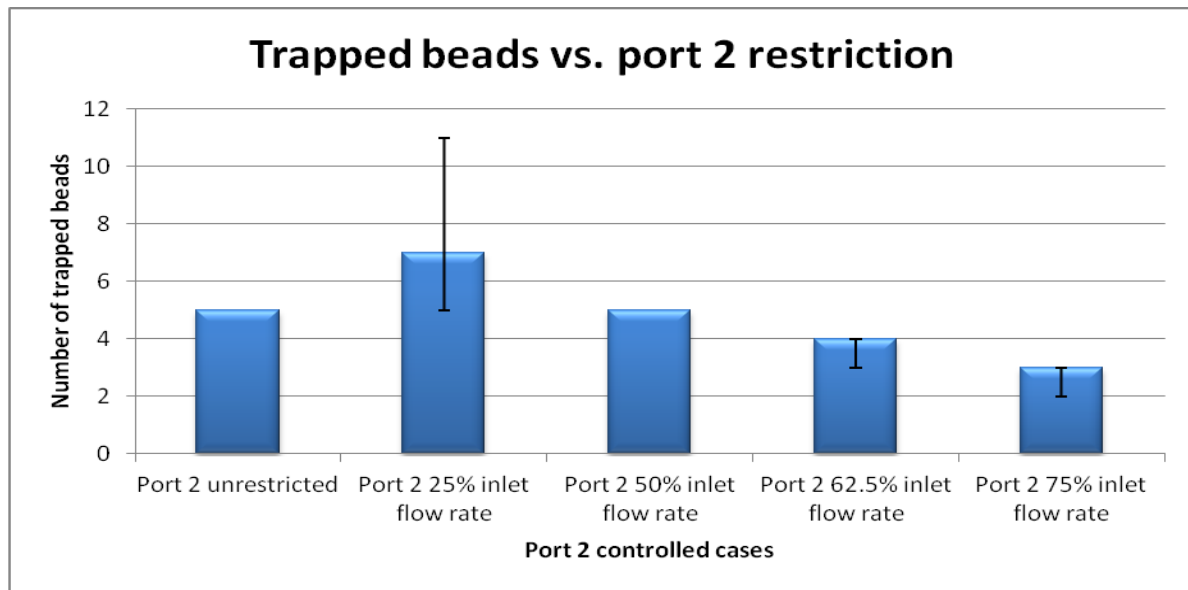


Figure 5.21: Experimental results of characterization with 20 μm beads for 5 different cases.

Mathematical models were performed using COMSOL for all of the conditions used during the characterization of the micro-fluidic device with 20 μm beads. The data collected from these models comprehends the pressure difference and the velocity ratio at the first available trap site assuming the beads are trapped in sequential order. The term first available trap site maybe confusing but this term refers only to the next vacant trap. If all traps are empty the first available trap site is the first trap, if there is a bead in the first trap the first available trap site is the second trap. The same happens for the remaining four traps. The first available trap site was very important in the research because we wanted to predict the behavior of the fluid inside the channel when the geometry of the channel changed. This is important because all the traps will not be fill at the same time most likely the traps will fill one by one and the conditions at the traps will vary when beads are trapped. Knowing how the conditions change we can have a better understanding of the operation of the channel.

The velocity ratio obtained from the data was defined as the ratio of the velocity through the available trap site (V_{trap}) and the velocity at the upper channel before the available trap site ($V_{channel}$). Figure 5.22 illustrates where the data was measured. Equation 33 shows the mathematical relation.

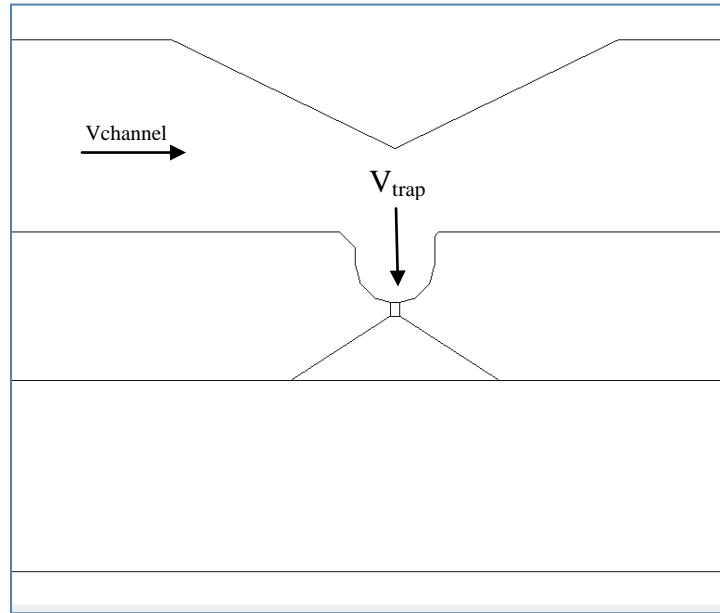


Figure 5.22: The region of the channel where V_{trap} and $V_{channel}$ were measured.

$$Velocity\ ratio = \frac{V_{trap}}{V_{channel}} \quad (33)$$

Figure 5.23 is a graphical representation of the modeled pressure difference between the upper channel and lower channel at the first available trap site for the condition of case 1. The results showed that the pressure difference between channels at the trapping sites decreases proportional to the distance between the first available trap and port 1. Figure 5.24 demonstrates that this trend is repeated in all of the cases that port 2 is controlled. It can be concluded that the pressure difference between the channels will always decrease and this

can represent a problem if the fluidic resistance of the channel at port 2 is too small. If the resistance is too small the pressure difference is not favorable to trap beads at the end of the channel.

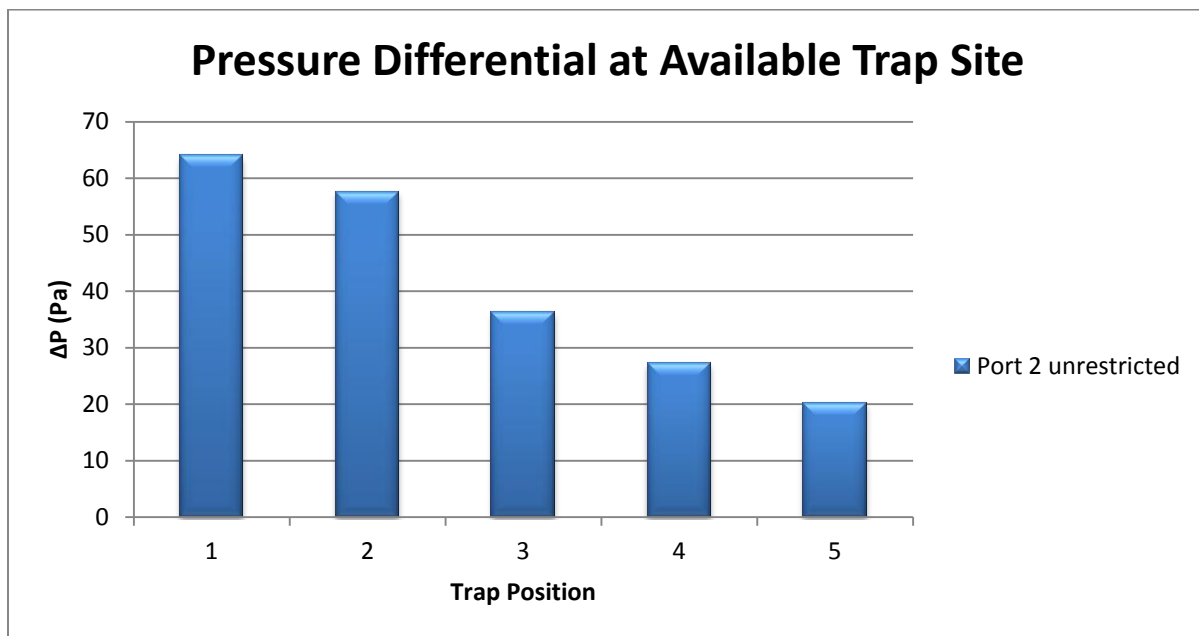


Figure 5.23: COMSOL results of the pressure differential (ΔP) at available trap site for case 1.

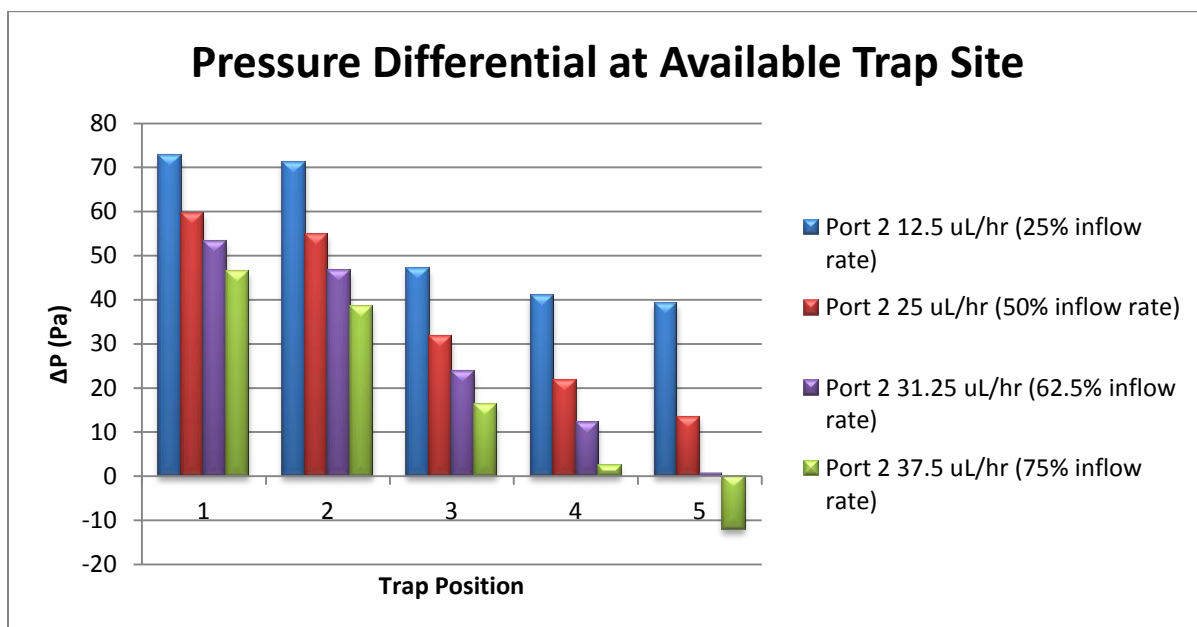


Figure 5.24: COMSOL results of the pressure differential (ΔP) at available trap site for cases 2, 3, 4 and 5.

The information of the velocity ratio at the first available trap site plus the micrographs of the experiments allowed deducing important functionality parameters. The graph of the velocity ratio at the first available trap site for case 1 (Figure 5.25) along with its corresponding micrograph (figure 5.16) showed that the trend of this ratio under these conditions tends to decrease. Although, the velocity ratio at available trap site is decreasing all the traps are filled with single particles. This means that the threshold to trap a 20 μm polystyrene bead is below the lowest value of the graph which is approximately 2.4. Figure 5.26 shows the trend of the velocity ratio for the other experimental conditions. The only case that has a different trend is when the flow through port 2 is restricted to 12.5 $\mu\text{L/hr}$ (case 2). In this case, the velocity ratio trend increases as the first available trap gets far from port 1. Comparing this case results to the micrographs (figure 5.17) it is possible to see that all of the

traps were filled but the last trap has multiple polystyrene beads. When the flow at port 2 was restricted to $25\mu\text{L/hr}$ (case 3), the micrograph (figure 5.18) showed single bead entrapment in all the trap sites and the trend of the velocity ratio is similar to case 1. Case 4 showed a decreasing trend with smaller values than the other cases. In fact the last trap has a negative velocity ratio which means that the flow at that trap is going upwards. The micrograph (figure 5.19) of this case shows that the 2 last traps are empty. A last case was studied in which the last bead was not retained (see figure 5.20) and the velocity ratio is near 1.37. This could imply that the threshold for single $20\ \mu\text{m}$ polystyrene bead entrapment in this device is 1.5. The information obtained from the COMSOL data and the micrographs it can be deduce that the minimum velocity ratio to trap a bead is near 1.5 and the maximum velocity ratio to avoid agglomeration is near 6. This parameter can hold the key to ensure bead entrapment without agglomeration in new and larger devices.

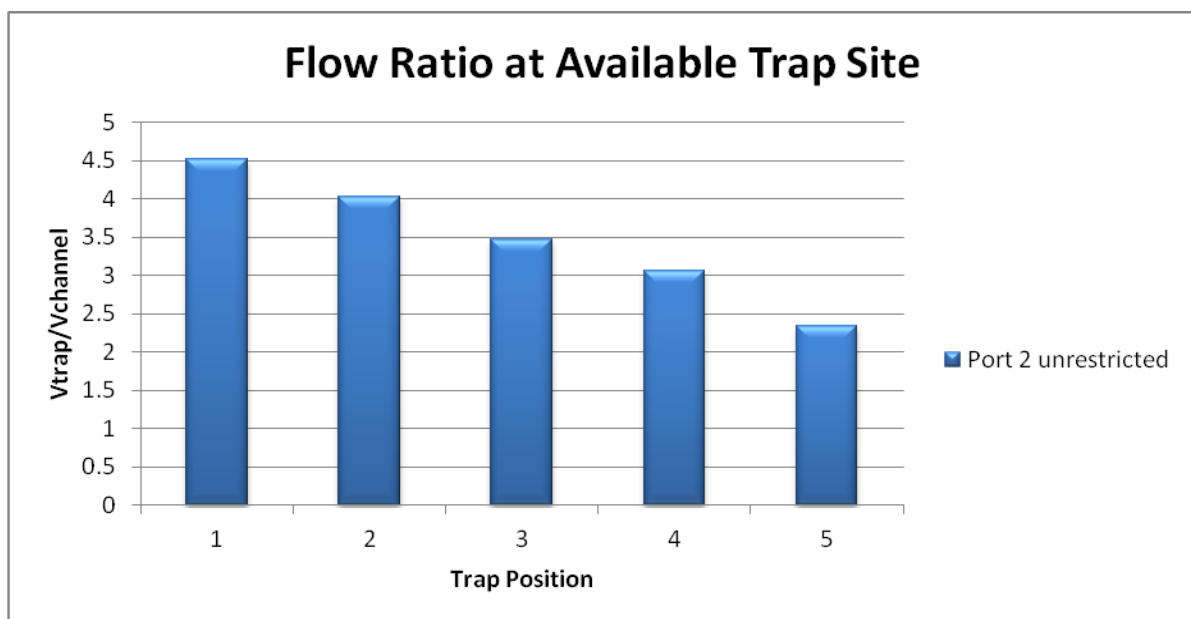


Figure 5.25: COMSOL results of the velocity ratio ($V_{\text{trap}}/V_{\text{channel}}$) at available trap site for case 1.

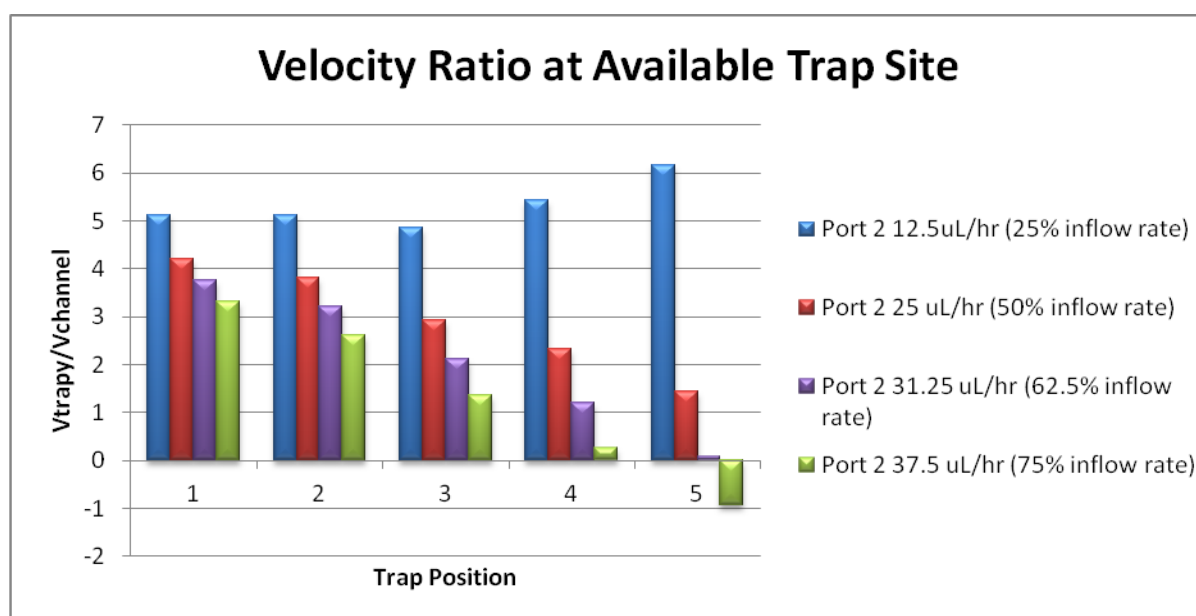


Figure 5.26: COMSOL results of the velocity ratio ($V_{\text{trap}}/V_{\text{channel}}$) at available trap site for case 2, case 3, case 4 and case 5.

Previous graphs showed the velocity ratio and pressure difference conditions of the cases studied. Figure 5.27 shows the velocity ratio at the first available trap site for a condition in which all the velocity ratio are similar. This theoretical condition was attained with a COMSOL model. It was determined that to attain this condition a flow restriction at port 2 of approximately $14.84\mu\text{L/hr}$ (29.7% of inflow rate) is necessary. Results show that this condition seems to be independent of the inflow rate. If a similar trend can be reached in a design with thousands of trap sites it is possible to induce $20\ \mu\text{m}$ polystyrene bead entrapments in all the trap sites. Figure 5.28 shows that the pressure difference at the trap sites has a decreasing trend just like in the other cases.

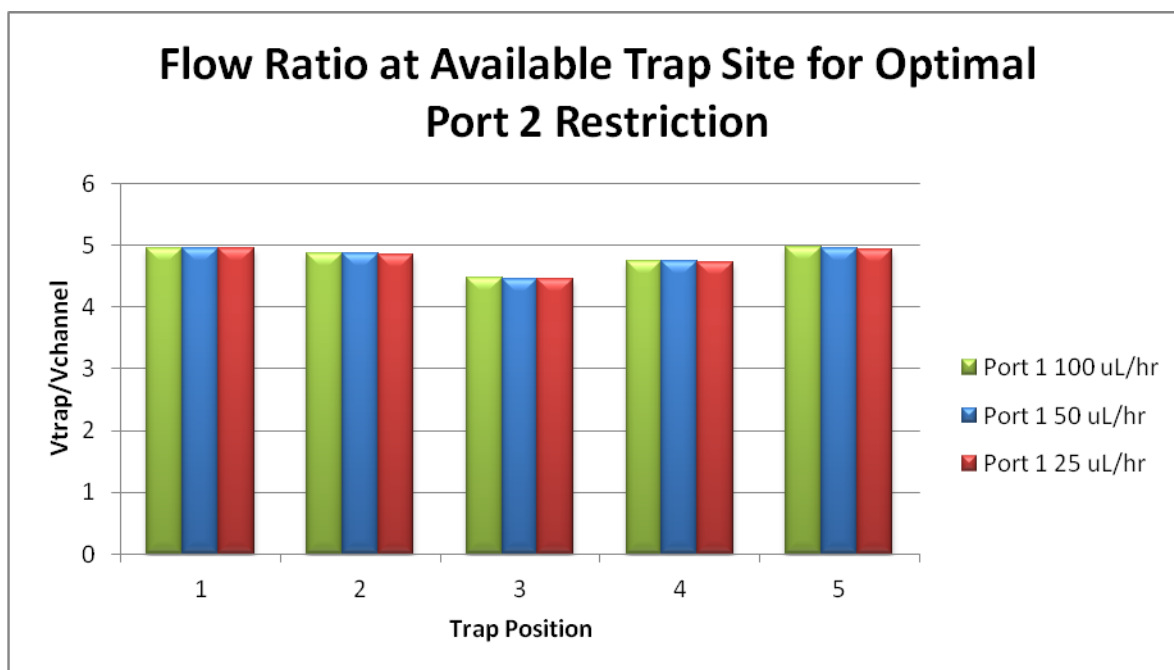


Figure 5.27: COMSOL results of the velocity ratio ($V_{\text{trap}}/V_{\text{channel}}$) at available trap site for case 6, case 7 and case 8.

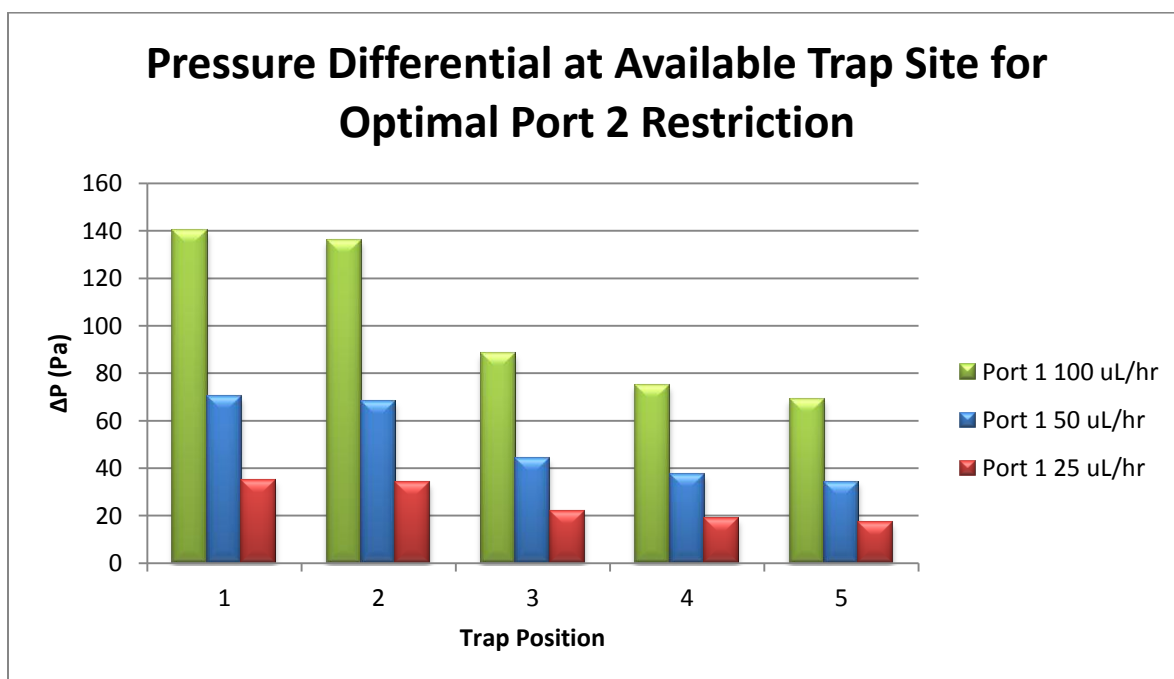


Figure 5.28: COMSOL results of the pressure differential (ΔP) at available trap site for case 6, case 7 and case 8.

CHAPTER 6

6.1 Conclusions

The experiments showed that the trapping efficiency is a strong function of the controlled output flow suggesting that the functionality of the device could be manipulated with a variable fluidic resistance. It was also found that the velocity profile of the computational model agrees well with experiments carried out with the micro-PIV, but only when there is a slip length of 13 μm at the PDMS walls and no slip at the glass wall. We suspect that the velocity slip is due to the surface treatment of the micro-channel walls (air plasma followed by bovine serum albumin functionalization). However, the evidence is not conclusive. The mass conservation experiments also helped confirmed that the asymmetrical slip length model is the best fit to describe the behavior of the fluidic medium inside the micro-fluidic device. There is evidence that due to the asymmetrical boundary conditions at the walls of the channel the maximum velocity of the fluid is shifted from the center of the channel to the top PDMS wall. Results from experimentation and COMSOL models indicate that the minimum velocity ratio to capture particles is approximately 1.5 and that the maximum ratio to avoid particle agglomeration is near 6. COMSOL data demonstrates that there is an operating condition that can yield similar velocity ratios in each trap site. This operating condition is independent of the inflow rate which means that only variations in the geometry of the channel will affect the operating condition. The validated computational model presented in this study will serve as a stepping stone for the development of high-

density cell isolation micro-devices for high-throughput single-cell electroporation applications and the detection of circulating tumor cells.

6.2 Future Work

In order to make an impact in single cell entrapment and research this study has to be extended to larger systems of high-density cell isolation. The next step in the course of this investigation is to design new geometries for micro-fluidic channels for high density cell isolation. These geometries will be analyzed with the mathematical model proposed in this thesis and the optimal operating parameters will be evaluated. Once fabricated, these new generation of micro-devices will be tested for single-cell electroporation and detection of circulating tumor cells. Figure 6.1 shows a prototype of such devices. Also, output condition can be varied with an array of micro-fluidic resistances that can be activated with pneumatic valves to produce different operating conditions.

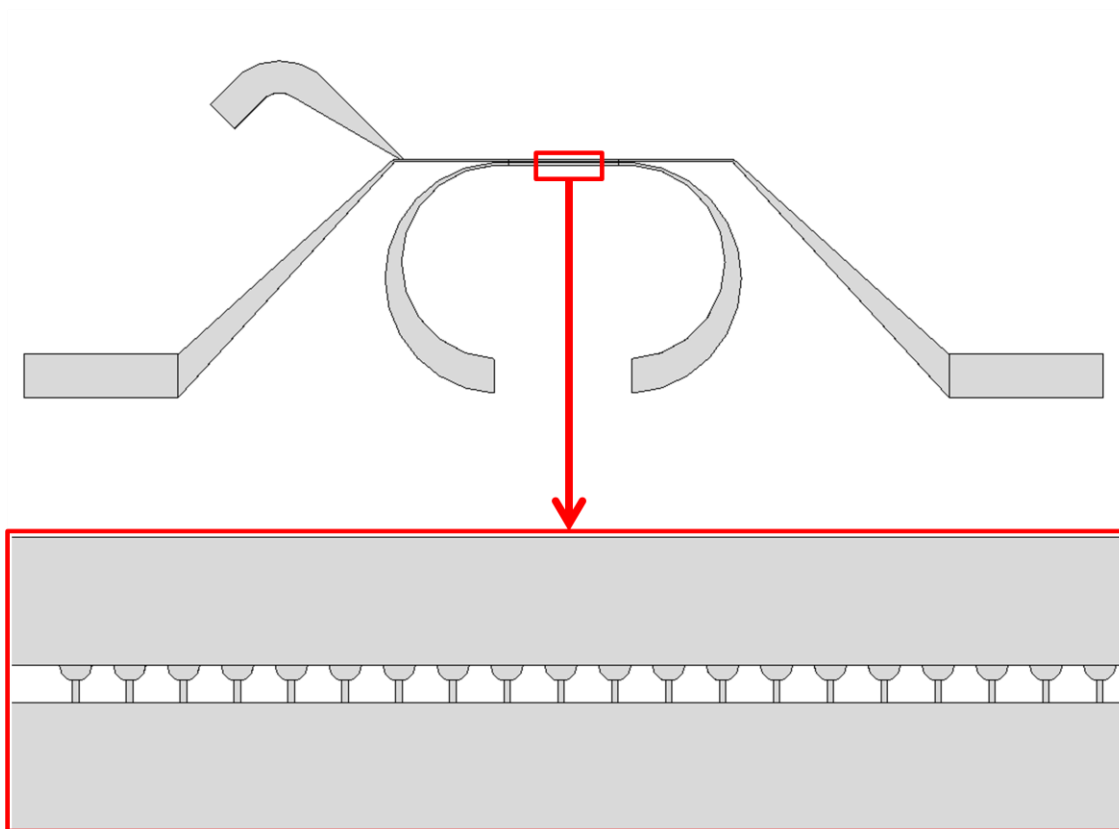


Figure 6.1: Prototype of micro-fluidic device for high-density cell isolation.

REFERENCES

1. Andersson, H., van den Berg, A. 2003. Microfluidic devices for cellomics: a review. *Sensors and Actuators B*. 92: 315-325.
2. McDonald, J. C., Duffy, D. C., Anderson, J. R., Chiu, D. T., Wu, H., Schueller, O. J. and Whitesides, G. M. 2000. Fabrication of microfluidic systems in poly(dimethylsiloxane). *Electrophoresis*. 21: 27-40.
3. Yi, C. Li, C., Yang, M. 2006. Microfluidics technology for manipulation and analysis of biological cells. *Analytica Chimica Acta*. 560: 1-23.
4. Sia, S. K. and Whitesides, G. M. 2003. Microfluidic devices fabricated in poly(dimethylsiloxane) for biological studies. *Electrophoresis*. 24: 3563-3576.
5. Chen, H., Sun, B., Tran, K., and Shen, H. 2009. A microfluidic manipulator for enrichment and alignment of moving cells and particles. *Journal of Biomechanical Engineering*. 131: 074505-1 - 074505-4
6. Yi, C., Li, C., Ji, S., and Yang, M. 2005. Microfluidics technology for manipulation and analysis of biological cells. *Analytica Chimica Acta*. 560: 1-23
7. Sochol, R. D., Iwai, K., Higa, A., Lo, J., Zhou, E., Lo, L., Luong, C., Dueck, M., Li, S., Lee, L., and Lin, L. 2010. A resettable high-density microfluidic cell trapping system. 14th International Conference on Miniaturized Systems for Chemistry and Life Sciences. 1574-1576.
8. Nilsson, J., Evander, M. and Laurell, T. 2009. Review of cell and particle trapping in microfluidic systems. *Analytica Chimica Acta*. 649: 141-157.
9. Yamada, M., and Seki, M. 2006. Microfluidic particle sorter employing flow splitting and recombining. *Analytical Chemistry*. 78(4): 1357-1362.
10. Tan, W. and Takeuchi, S. 2007. A trap-and-release integrated microfluidic system for dynamic microarray applications. *PNAS*. 4: 1146-1151.

11. Takagi, J., Yamada, M., Yasuda, M., and Seki, M. 2005. Continuous particle separation in a microchannel having asymmetrically arranged multiple branches. *Lab Chip*. 5: 778-784.
12. Choi, S., Lee, M., and Park, J. 2010. Microfluidic parallel circuit for measurements of hydraulic resistance. *Biomicrofluidics*. 4: 034110-1 - 034110-9.
13. Judy, J., Maynes, D., and Webb, B.W. 2002. Characterization of frictional pressure drop for liquid flows through microchannels. *International Journal of Heat and Mass Transfer*. 45:3477-3489.
14. Wheeler, A. R., Thronset, W. R., Whelan, R. J., Leach, A. M., Zare, R. N., Liao, Y. H., Farrell, K., Manger, I. D., and Daridon, A. 2003. Microfluidic Device for Single-Cell Analysis. *Anal. Chem*. 75: 3581-3586.
15. Roman, G. T., Chen, Y., Viberg, P., Culbertson, A. H. and Culbertson, C. T. 2007. Single-cell manipulation and analysis using microfluidic devices. *Anal Bioanal Chem*. 387: 9-12.
16. Arakawa, T., Noguchi, M., Sumitomo, K., Yamaguchi, Y. and Shoji, S. 2011. High-throughput single-cell manipulation system for a large number of target cells. *Biomicrofluidics*. 5: 014114.
17. Kirby, B. 2010. *Micro- and Nanoscale Fluid Mechanics Transport in Microfluidic Devices*. First Edition. Cambridge University Press
18. Munson, B., Young, D. and Okiishi, T. 2006. *Fundamentals of Fluid Mechanics*. Fifth Edition. John Wiley & Sons
19. Neto, C., Evans, D., Bonaccorso, E., Butt, H. and Craig, V. 2005. Boundary slip in Newtonian liquids: a review of experimental studies. *Rep. Prog. Phys*. 68: 2859-2897
20. Tibbs, K. W., Baras, F. and Garcia, A. L. 1997. Anomalous flow profile due to the curvature effect on slip length. *Phys. Rev. E* 56: 2282–2283
21. Barrat, J-L. and Bocquet, L. 1999. Large slip effect at a nonwetting fluid–solid interface. *Phys. Rev. Lett*. 82: 4671–4674

22. Melling, A. 1997. Tracer particles and seeding for particle image velocimetry. *Measurement Science and Technology*. 8: 1406-1416.
23. Barrat, J-L. and Bocquet, L. 1999. Influence of wetting properties on hydrodynamic boundary conditions at a fluid/solid interface. *Faraday Discuss.* 112: 119–127
24. Ou, J., Perot, B. and Rothstein, J. P. 2004. Laminar drag reduction in microchannels using ultrahydrophobic surfaces. *Phys. Fluids* 16: 4635–4643
25. Ishida, N., Inoue, T., Miyahara, M. and Higashitani, K. 2000. Nano bubbles on a hydrophobic surface in water observed by tapping mode atomic force microscopy. *Langmuir*. 16: 6377–6380
26. Tyrrell, J. W. G. and Attard, P. 2001. Images of nanobubbles on hydrophobic surfaces and their interactions. *Phys. Rev. Lett.* 87: 176104
27. Sakamoto, M., Kanda, Y., Miyahara, M. and Higashitani, K. 2002. Origin of long-range attractive force between surfaces hydrophobized by surfactant adsorption. *Langmuir*. 18: 5713–5719
28. Christenson, H. K. and Claesson, P. M. 2001. Direct measurements of the force between hydrophobic surfaces in water. *Adv. Colloid Interface Sci.* 91: 391–436
29. Henry, C. L., Neto, C., Evans, D. R., Biggs, S. and Craig, V. S. 2004. The effect of surfactant adsorption on liquid boundary slippage. *Physica A* 339: 60–65
30. Zhu, Y. and Granick, S. 2002. No-slip boundary conditions switches to partial slip when fluid contains surfactant. *Langmuir*. 18: 10058–10063
31. Jensen, T. R., Jensen, M. O., Reitzel, N., Balashev, K. and Peters, G.H. 2003. Water in contact with extended hydrophobic surfaces: direct evidence of weak dewetting. *Phys. Rev. Lett.* 90: 86101
32. Lauga, E. and Brenner, M. P. 2004. Dynamic mechanism for apparent slip on hydrophobic surfaces *Phys. Rev. E* 70: 26311

33. Lindken, R., Rossi, M., Grobe, S. and Westerweel, J. 2009. Micro-Particle Image Velocimetry (μ PIV): Recent developments, applications, and guidelines. *Lab on a Chip*. DOI: 10.1039/b906558j
34. Guasto, J. S., P. Huang and K. S. Breuer. 2006. Statistical particle tracking velocimetry using molecular and quantum dot tracer particles. *Experiments in Fluids* 41(6): 869-880.
35. Santiago, J.G. , Wereley S.T., Meinhart, C.D., Beebe, D.J., and Adrian, R.J. 1998. A Particle Image Velocimetry System for Microfluidics, *Experiments in Fluids*. 25, 4: 316-319
36. Olsen, M. G. and Adrian, R. J. 2000. Out-of-focus effects on particle image visibility and correlation in microscopic particle image velocimetry. *Exp. Fluids*. 29: S166-S174.
37. Gale, J., Romero, C., Tafoya, G., and Conia, J. 2003. Application of optical trapping for cells grown on plates: optimization of PCR and fidelity of DNA sequencing of p53 gene from a single cell. *Clinical Chemistry*. 49: 415-424.
38. Gerhardt, T., Woo, S., and Ma, H. 2011. Chromatographic behaviour of single cells in a microchannel with dynamic geometry. *Lab Chip*.
39. López-Martínez, M. 2011. Characterization of a Microfluidic Device for Autonomous Biological Cell Entrapment and Electrical Interrogation. University of Puerto Rico Mayaguez Campus.
40. Thormann, E., Simonsen, A., Hansen, P., and Mouritsen, O. 2008. Interactions between a Polystyrene Particle and Hydrophilic and Hydrophobic Surfaces in Aqueous Solutions. *Langmuir*. 24: 7278-7284.
41. Lei, W., Jiankang, W. and Bo, C. 2009. Analytic Solution of Liquid Flow in Rectangular PDMS-GLASS Microchannel with Wall Slip and Electro-Viscous Effects. *Applied Mathematical Sciences*. 3: 2195-2214